Physics of Fluids

RESEARCH ARTICLE | APRIL 05 2021

Parametric sensitivities of the generalized binomial Langevin–multiple mapping conditioning model

Special Collection: In Memory of Edward E. (Ted) O'Brien

Matthew du Preez ; Andrew P. Wandel ; D. Bontch-Osmolovskaia; R. Peter Lindstedt

Physics of Fluids 33, 045109 (2021)
https://doi.org/10.1063/5.0041351

Physics of Fluids ARTICLE scitation.org/journal/phf

Parametric sensitivities of the generalized binomial Langevin–multiple mapping conditioning model

Cite as: Phys. Fluids 33, 045109 (2021); doi: 10.1063/5.0041351
Submitted: 22 December 2020 · Accepted: 4 March 2021 ·
Published Online: 5 April 2021

Matthew du Preez,[1] Andrew P. Wandel,[1,a)] D. Bontch-Osmolovskaia,[1] and R. Peter Lindstedt[2]

AFFILIATIONS

[1]School of Mechanical and Electrical Engineering, University of Southern Queensland, Toowoomba, Queensland 4350, Australia
[2]Department of Mechanical Engineering, Imperial College, Exhibition Road, London SW7 2AZ, United Kingdom

Note: This paper is part of the special topic, In Memory of Edward E. (Ted) O'Brien.
[a)]**Author to whom correspondence should be addressed:** andrew.wandel@usq.edu.au

ABSTRACT

The binomial Langevin model (BLM) predicts mixture fraction statistics including higher moments excellently, but imposing boundedness for the large scalar spaces typically associated with chemically reacting flows becomes intractable. This central difficulty can be removed by using the mixture fraction as the reference variable in a generalized multiple mapping conditioning (MMC) approach. The resulting probabilistic BLM–MMC formulation has several free parameters that impact the turbulence–chemistry interactions in complex flows: the dissipation timescale ratio, the locality in selecting pairs of particles for mixing, and the fraction of particles mixed per time step. The impact of parametric variations on the behavior of the BLM–MMC model is investigated for a complex flow featuring auto-ignition to determine model sensitivities and identify optimal values. It is shown that only the mixture fraction rms is sensitive to the dissipation timescale ratio with the expected behavior of an increased ratio leading to a reduction in rms. Controlling locality by increasing the maximum possible distance between paired particles in reference space has a similar impact. Increasing the fraction of particles mixed only affects reacting scalars by advancing ignition. The modified Curl's model is used for the mixing process and the specified amount of mixing principally controls the local extinction and reignition behavior. It is further shown that the standard value of the dissipation timescale ratio is satisfactory; the amount of mixing should be half that specified by Curl's model; and the distance between particle pairs in reference space should be proportional to the diffusion length scale.

I. INTRODUCTION

One of the promising methods for reducing emissions from combustion-based devices is to use lean mixtures of fuel that are close to device stability limits. Flame stabilization is an important feature to be controlled in engines operating under such conditions[1–4] where the time-dependent combustion behavior may cause flame instability[5–8] due to the pressure-convection coupling. Under such conditions, finite-rate chemistry has a significant influence with phenomena such as extinction/reignition emerging as turbulence–chemistry interactions become dominant.[9–14] In seminal work, Dopazo and O'Brien[15,16] presented a modeled equation for the joint probability density function (PDF) of a set of scalars that incorporated mixing and chemical reaction with application to autoignition of a turbulent mixture.[15] In order to capture such effects, it is necessary to consider a wide range of timescales,[17,18] and transported PDF models are well suited for these applications.[19,20] A key consideration in implementing PDF models for these types of flows is that the predictions of bulk quantities become sensitive to model parameters, especially the molecular mixing closure.[21]

The multiple mapping conditioning (MMC) approach[22–25] has the potential to address these challenges. It has been applied to model experimental cases that display extinction/reignition in different forms[26,27] with some success.[28–34] The basis for MMC is that the multi-dimensional scalar space can be represented by a lower-dimensional manifold.[35] In Conditional Moment Closure (CMC),[36] this lower-dimensional manifold is mapped onto a one- or two-dimensional manifold; in non-premixed combustion, the mixture fraction is always used as a dimension, while either sensible enthalpy or scalar dissipation can be used as a secondary dimension. In MMC, this low-dimensional CMC manifold is mapped onto a reference space,

which is typically one-dimensional. To model extinction/reignition phenomena, a single reference space dimension is insufficient to represent all the behavior because the chemical timescales are longer than the turbulent timescales, while the fluid can originate from either the burnt or unburnt regions. Therefore, the deviations from the conditional mean must be modeled ("probabilistic MMC"[37]) These conditional fluctuations have a relaxation timescale τ_{min}—mathematically similar to the relaxation timescale τ_{maj} of unconditional fluctuations to the global mean—that must be specified to implement probabilistic MMC.[38]

Conventional MMC specifies that the PDF of the reference variable is Gaussian; most implementations of MMC apply this specification.[30–32,34,38,39] A fundamental challenge for conventional MMC is the modeling of the interaction of the mathematical reference variable with physical variables such as velocity. Generalized MMC[40] permits any variable to be the reference variable, so it is possible to use a physical variable with the same statistical properties as the variable that is used as the basis for all scalars. The application of generalized MMC has typically been to non-premixed combustion with the mixture fraction used as the basis for the mixing of all the scalars. The current examples describe partially premixed combustion, which contain physics that are a combination of non-premixed and premixed flames, although the driving mechanism to create these situations is the same process as non-premixed combustion. The reference variable mixture fraction controls the mixing behavior of the MMC mixture fraction; the latter governs the mixing behavior of all the other scalars. The objective of the method is to determine which pairs of particles to mix to create a chemical composition that models a statistically homogeneous spatial region. The particles are stochastically advected while the chemical state is deterministic. Two implementations of generalized MMC have been developed. Both implementations use stochastic particles to represent the joint-PDF of the mixture fraction, reactive scalars, and velocity; all processes in the PDF transport equation are deterministic except for the model for turbulent mixing. One implementation of generalized MMC is for large Eddy simulations (LES), where the filtered mixture fraction of the LES field is used as the reference variable for the MMC mixture fraction associated with each stochastic particle;[41] all LES implementations of MMC are derived from this model. The other is for Reynolds-averaged Navier–Stokes (RANS) models, where the binomial Langevin model (BLM)[42] is solved for each stochastic particle; the BLM velocity was originally used as the reference variable,[29,43] but now the BLM mixture fraction is preferred (BLM-MMC).[33]

A remaining challenge for the generalized BLM-MMC model is to link the control of the conditional fluctuations (via the mixing model parameters) to the relevant mixing timescale τ_{min}. The theoretical development of a model for τ_{min} specifies that it should be proportional to τ_{maj}.[38,39] For implementations based on interaction by exchange with the conditional mean (IECM), the implementation of τ_{min} within the model is clear. However, use of the modified Curl's (MC) model[44,45] within MMC poses a challenge for the direct implementation of τ_{min}. One solution is to define the amount of mixing using the IECM formulation;[30] this methodology has been applied in all subsequent implementations of MMC in a RANS context, except those by the authors. The fundamental difference is that the current implementation follows the approach of Wandel[39] by randomly selecting pairs of particles for mixing, so that the pair is separated by no more than a diffusion length-scale within the reference space with a random subset of particles mixed for any given time step. Other implementations pair neighboring particles in reference space with all particles mixed at every time step.

This fundamental difference in implementations of MMC to RANS, outlined above, causes different approaches to the modeling of turbulent intermittency. The latter is caused by the transport by intermediate-sized vortices. Other approaches rely on the number of stochastic particles and the computational time step to be sufficiently high so that the particles are reordered in reference space, with the mixing intensity for each interaction being relatively low. The current authors' approach is numerically valid for smaller numbers of particles and/or time steps, with the mixing intensity for each interaction being relatively high.

The current article provides a comprehensive analysis of the impact of each of the free parameters in BLM-MMC on the computational results for a complex test case featuring auto-ignition in a turbulent flow field.

II. THEORY

This section describes all the relevant theory required for implementing BLM-MMC.

A. Scalar dissipation timescales

The unconditional fluctuations of the scalar Z are defined to be

$$Z' = Z - \langle Z \rangle, \tag{1}$$

with $\langle Z \rangle$ the unconditional mean, which can be calculated by averaging over stochastic particles. The dissipation term in the transport equation for the variance of Z is unclosed:

$$\frac{\partial \langle Z'^2 \rangle}{\partial t} = -2\left\langle D \frac{\partial Z}{\partial x_i}\frac{\partial Z}{\partial x_i} \right\rangle, \tag{2}$$

where D is the molecular diffusivity of Z and the Einsteinian summation convention is applied. The scalar dissipation rate is defined to be

$$N \equiv D \frac{\partial Z}{\partial x_i}\frac{\partial Z}{\partial x_i}; \tag{3}$$

this definition is preferred to the common definition $\chi = 2N$ since N is more convenient in CMC/MMC formulations.

To close Eq. (2), a model for the mean scalar dissipation is required. The most commonly used model is to assume that the dissipation rate of velocity is proportional to the dissipation rate of scalars,

$$\langle N \rangle = C_Z \frac{\varepsilon}{k} \langle Z'^2 \rangle. \tag{4}$$

Here, k is the turbulent kinetic energy, ε is the turbulent kinetic energy dissipation rate, and the constant C_Z normally[46] takes the value 1.0, although it may be tuned to suit a model for a particular case. The relevant timescale for the dissipation of the unconditional fluctuations is the "major" dissipation timescale τ_{maj}

$$\langle N \rangle \equiv \frac{\langle Z'^2 \rangle}{\tau_{maj}}. \tag{5}$$

The major dissipation timescale is therefore conventionally modeled as

$$\tau_{\text{maj}} = \tau_u / C_Z, \tag{6}$$

where $\tau_u \equiv k/\varepsilon$ is the turbulent dissipation timescale. The effect of C_Z on BLM-MMC is investigated in Sec. III C

The conditional fluctuations of the scalar Y are defined to be

$$Y'' \equiv Y - \langle Y|Z\rangle, \tag{7}$$

with $\langle Y|Z\rangle$ the conditional mean: the mean of Y with the condition that the independent ("conditioning") variable Z takes a particular value. The conditional variance $\langle Y''^2|Z\rangle$ can be integrated to yield the (unconditional) mean conditional variance,

$$\langle Y''^2\rangle \equiv \int_{-\infty}^{\infty} \langle Y''^2|Z\rangle P_Z(Z) dZ, \tag{8}$$

where $P_Z(Z)$ is the PDF of Z. The mean of the conditional variance is not the same as the mean of the unconditional variance (note that the unconditional variance is already an unconditional moment, so taking the mean of the unconditional variance produces the same value). The difference between the mean conditional variance and unconditional variance was derived by Wandel[39] (see the Appendix B). The dissipation rate of the conditional fluctuations is defined to be

$$\Psi_D \equiv \left\langle D \frac{\partial Y''}{\partial x_i} \frac{\partial Y''}{\partial x_i} \middle| Z \right\rangle \tag{9}$$

and can be modeled using

$$\langle \Psi_D\rangle \equiv \frac{\langle Y''^2\rangle}{\tau_{\text{min}}}. \tag{10}$$

The minor dissipation timescale τ_{min} is a measure of the rate of decay of the conditional fluctuations. This decay occurs in practice because there is a physical separation between a point at x_1 with value of scalar $Y(x_1)$ and a location x_2 where the scalar $Y(x_2)$ is the same as the conditional mean of Y at location x_1: $Y(x_2) = \langle Y|Z(x_1)\rangle$. There is a corresponding physical separation between x_1 and a location x_3 where $Y(x_3)$ is the unconditional mean: $Y(x_3) = \langle Y\rangle$. Because $\langle|x_1 - x_2|\rangle$ is significantly shorter than $\langle|x_1 - x_3|\rangle$, $\tau_{\text{min}} < \tau_{\text{maj}}$, and τ_{min} is a "micro-dissipation timescale" (it governs the small scales of turbulence), while τ_{maj} is a "macro-dissipation timescale" (it governs the large scales of turbulence).[18] If the conditional fluctuations are negligible (i.e., $|x_1 - x_2| \to 0$), then $\tau_{\text{min}} \ll \tau_{\text{maj}}$. The value of τ_{min} is influenced by turbulence–chemistry interactions, but also by how the conditioning space is defined, because τ_{min} is a measure of the magnitude of the conditional fluctuations.[29] If the conditioning space has more dimensions (i.e., there are more reference variables), then it is possible to reduce the conditional fluctuations. A good choice of the reference variables will mean the reference space does not require many dimensions for $\tau_{\text{min}} \ll \tau_{\text{maj}}$ to occur.[25] This occurs when the dimensionality of all scalars represented by Z is no smaller than the number of independent dimensions in the multi-dimensional space represented by all Y. In other words, Y-space can be represented by a manifold generated by Z-space[18] because there are sufficient dimensions in Z-space to govern the dimensions in Y-space. This representation is possible by considering that the scalar variables construct a space where each variable is a dimension, and the values of all the scalars at a specific point in physical space are mapped to the corresponding point in the scalar space.[25] In circumstances where the conditional fluctuations are non-negligible (typically because local extinction/reignition results in the manifold being at least two-dimensional, while a single dimension is used for conditioning), the following value[38] is normally used to model τ_{min} within MMC:

$$\frac{\tau_{\text{min}}}{\tau_{\text{maj}}} = \frac{1}{8}. \tag{11}$$

This value was selected as it provided the best match to the DNS data provided by Mitarai *et al.*[47] in a study of local extinction/reignition, and also produced superior results to the other turbulent combustion models tested.[48] Subsequent implementations of MMC by other groups have also found that this value produces optimal results.

Equation (10) is one of the terms in second-order CMC.[36] A challenge for CMC is that $P_Z(Z)$ requires modeling; producing an accurate representation of the actual PDF is challenging for many cases. In the MMC framework, an additional level of conditioning is used, where the Z-space (used to condition Y) is mapped to ξ-space, where ξ can be any variable. The relevant conditional fluctuations are

$$Z''' \equiv Z - \langle Z|\xi\rangle. \tag{12}$$

These are related to the ratio (q) of the dissipation timescales by[39]

$$q = \frac{\tau_{\text{min}}}{\tau_{\text{maj}}} = \frac{\langle Z'''^2\rangle}{\langle Z'^2\rangle}, \tag{13}$$

so calculation of the variances is sufficient for determining the value of τ_{min} for a given realization. The relevant minor dissipation timescale takes the same value[40] as the timescale defined in Eq. (10), so it not necessary to calculate Y'' when implementing probabilistic MMC.

B. Generalized MMC

In conventional MMC, ξ is chosen to have a standard Gaussian distribution, which results in a mathematically well-defined PDF $P_\xi(\xi)$, but requires the mapping function $Z = X(\xi)$ to be modeled; a satisfactory universal model for the inhomogeneous drift term has yet to be derived. In generalized MMC,[40] ξ is normally chosen to be the same variable as Z, but calculated independently, so both the PDF and the mapping function are well-defined. The transport equation for ξ is therefore model-dependent and for BLM-MMC the relevant details for transport are described in Sec. II C.

The transport equations for the scalars associated with stochastic particle p (where $*$ denotes a stochastic trajectory) are

$$dZ^{*p} = S dt, \tag{14}$$

$$dY_I^{*p} = (S + W_I) dt, \tag{15}$$

where S denotes molecular mixing determined using a mixing model that provides a closure for the dissipation of the scalar PDF, and W is the chemical source term for scalar I. Equations (14) and (15) imply the common assumption of equal rates of mixing for all scalars and hence an appropriately high turbulent Reynolds number, although this does not preclude the possibility of S accounting for differential diffusion. A key requirement of S is that it is local in reference space, i.e., only those particles with values of ξ that are close to the particle value ξ^{*p} are able to influence S for particle p. The modified Curl's model[44,45] is used for S in BLM–MMC, as described in Sec. II D.

Particles are transported in physical space according to

$$dx_i^{*p} = u_i^{*p} dt, \tag{16}$$

where u_i^{*p} must be consistent with the transport of ξ^{*p}.

C. Binomial Langevin model

The form of the binomial Langevin model[42] used in BLM-MMC is for the joint-PDF of velocity and scalars.[49] The transport equation for the velocity u_i is

$$du_i^{*p} = \frac{1}{\tau_u}\left(\alpha_1\delta_{ij} + \alpha_2\beta_{ij}\right)\left(u_j^{*p} - \langle u_j\rangle\right)dt + \left(C_0\langle\varepsilon\rangle\right)^{1/2} d\omega_i, \tag{17}$$

where $d\omega_i$ is an isotropic Wiener process and the Reynolds stress anisotropy tensor is

$$\beta_{ij} = \frac{\langle u_i' u_j'\rangle}{\langle u_k' u_k'\rangle} - \frac{\delta_{ij}}{3}. \tag{18}$$

The applied modeling coefficients are $C_0 = 2.1$, $\alpha_2 = 3.7$ and $\alpha_1 = -\left(\frac{1}{2} + \frac{3}{4}C_0\right) - \alpha_2\beta_{ll}^2$.

In BLM-MMC, the mixture fraction from the transport equation

$$d\xi^{*p} = Adt + \left(2\langle N\rangle\mathcal{B}_\xi\right)^{1/2} d\omega_{\text{bin}} \tag{19}$$

is used as the reference variable.

The drift and diffusion coefficients in Eq. (19) are

$$A = \frac{G_\xi}{\tau_{\text{maj}}}\left(\xi^{*p} - \langle\xi\rangle\right), \tag{20}$$

$$G_\xi = -\left\{K_\xi\left[1 - \left\langle\left(\frac{\xi'^{(*p)}}{\xi_*'}\right)^2\right\rangle\right] + 1\right\}, \tag{21}$$

$$\mathcal{B}_\xi = K_\xi\left[1 - \left(\frac{\xi'^{(*p)}}{\xi_*'}\right)^2\right], \tag{22}$$

where

$$K_\xi = K_0\left(1 - \frac{\theta_\xi}{|\theta_\xi| + 1}\right), \tag{23}$$

$$\theta_\xi = C_K\frac{\left[\left(\xi^{*p} - \langle\xi\rangle\right)\left(u_i^{*p} - \langle u_i\rangle\right) - \langle\xi' u_i'\rangle\right]\langle\xi' u_i'\rangle}{\frac{2}{3}\langle k\rangle\langle\xi'^2\rangle}, \tag{24}$$

and $K_0 = 2.1$ and $C_K = 0.76$. Note that Eq. (24) provides the mechanism for u_i^{*p} to be consistent with the transport of ξ^{*p}. Furthermore,

$$\xi'^{(*p)} = \xi^{*p} - \langle\xi\rangle^{*p}, \tag{25}$$

$$\xi_*' = \begin{cases} \xi_{\max}'^{(*p)}, & \xi'^{(*p)} > 0 \\ \xi_{\min}'^{(*p)}, & \xi'^{(*p)} < 0 \end{cases}, \tag{26}$$

$$\langle\xi\rangle^{*p} = \xi_{\min}|_{\xi=\xi^{*p}} + \left(\langle\xi\rangle - \xi_{\min}|_{\xi=\xi^{*p}}\right) \times \frac{\xi_{\max}|_{\xi=\xi^{*p}} - \xi_{\min}|_{\xi=\xi^{*p}}}{\xi_{\max}|_{\xi=\langle\xi\rangle} - \xi_{\min}|_{\xi=\langle\xi\rangle}}, \tag{27}$$

where $\xi_{\min}|_{\xi=\xi^{*p}}$ is the smallest possible value of ξ given the value ξ^{*p}, while $\xi_{\max}|_{\xi=\xi^{*p}}$ is the largest possible value.

The binomial Langevin Wiener process in Eq. (19) obeys[42]

$$d\omega_{\text{bin}} = \frac{b - MQ}{\sqrt{MQ(1-Q)}\sqrt{dt}}, \tag{28}$$

where b is an integer sampled from the binomial distribution with PDF $P_b(b; M, Q)$, where M is the total number of trials and Q is the probability of the bth trial being successful:

$$P_b(b; M, Q) = \binom{M}{b} Q^b (1-Q)^{M-b}, \tag{29}$$

$$M = \frac{\left(\xi_{\max}'^{(*p)} - \xi_d\right)\left(\xi_d - \xi_{\min}'^{(*p)}\right)}{2\langle N\rangle\mathcal{B}_\xi dt}, \tag{30}$$

$$Q = \frac{\xi_d - \xi_{\min}'^{(*p)}}{\xi_{\max}'^{(*p)} - \xi_{\min}'^{(*p)}}, \tag{31}$$

$$\xi_d = \xi^{*p} - Adt. \tag{32}$$

Because both the scalar Z and its reference variable ξ are mixture fractions, the mapping function is theoretically:

$$E(Z|\xi) \equiv X(\xi) = \xi. \tag{33}$$

If $Z''' = 0$, then $\langle Z|\xi\rangle = X$ and conditional MMC modeling is performed; in BLM-MMC, Z''' is allowed to deviate from 0 and the magnitude of Z''' is to be controlled.

The principal benefits of using BLM are (i) that it models the mixture fraction PDF with a high degree of accuracy,[49] so provides the necessary basis for an accurate mapping of the mixture fraction Z and hence high-fidelity modeling of the PDF of Z. In addition, (ii) BLM ensures the necessary consistency between u_i and ξ by solving the joint-PDF of those variables.

D. Modified Curl's model

If two stochastic particles have different weights w^{*p} (i.e., each stochastic particle has a different probability of existing, so a weighted average of particle properties is required to obtain any type of average of a variable), then the MC[44,45] mixing of particles p and q for any variable ϕ between time step k and time step $k+1$ can be expressed as

$$\phi_{k+1}^{*p} = \phi_k^{*p} + \frac{w^{*q}}{w^{*p} + w^{*q}}\alpha\left[\phi_k^{*q} - \phi_k^{*p}\right], \tag{34}$$

$$\phi_{k+1}^{*q} = \phi_k^{*q} - \frac{w^{*p}}{w^{*p} + w^{*q}}\alpha\left[\phi_k^{*q} - \phi_k^{*p}\right], \tag{35}$$

where $0 \le \alpha \le 1$ is the fraction of mixing (0 represents no mixing, while 1 represents complete mixing to the weighted mean: Curl's model[50]) The amount by which variable ϕ^{*p} changes is proportional to the (statistical) weight of the other particle w^{*q} so that the (weighted) mean of ϕ is constant during the mixing process. The weight w^{*p} can be interpreted as the probability of particle p existing relative to particle q.

The fraction of mixing (α) can be a random variable with a PDF,[44,45] denoted $P_\alpha(\alpha)$. The simplest possible PDF is $P_\alpha(\alpha) = \delta(\alpha - \alpha_0)$, where $\alpha_0 = \langle\alpha\rangle$ is a fixed value of mixing; another commonly used PDF is a uniform distribution (for $\langle\alpha\rangle = 0.5$). For these

two PDFs, it has been found[39] that mean statistics calculated by MC (e.g., temperature) are independent of the shape of $P_\alpha(\alpha)$ if the value of $\langle\alpha\rangle$ is the same. However, conditional statistics (e.g., stoichiometric temperature) change for different shapes of $P_\alpha(\alpha)$. The effect of the value of $\langle\alpha\rangle$ and the shape of $P_\alpha(\alpha)$ are studied in Sec. III D.

In the original Curl's model[50] and MC,[44,45] a fraction of the particles mix in any given time step. This fraction can be defined as a probability that particles mix, $\mathcal{P}_m$, and is well-defined for MC because a formula that is a function of $P_\alpha(\alpha)$ can be derived based on the constraint Eq. (2) and the closure model Eq. (4). The value of $\mathcal{P}_m$ for MMC is less clear because it is a non-linear function of the parameters. In other RANS implementations of MMC,[30,31,51] the choice $\mathcal{P}_m = 1$ is made, which constrains $\langle\alpha\rangle$. In those models[30,51] which have uniform w^{*p}, $P_\alpha(\alpha) = \delta(\alpha - \alpha_0)$, where α_0 is a function of Δt and $\tau_{\min}$. The other model[31] (also used elsewhere[52]) allows particles to have unique values of w^{*p}, so α_0 is also a function of w^{*p} and w^{*q}. Wandel[39] determined that for homogeneous flows the optimal value is $\langle\alpha\rangle = \frac{1}{2}$ because it generates the correct levels of conditional fluctuations. This means that the value of $\mathcal{P}_m$ remains open; its effect on the flow is investigated in Sec. III F.

E. Selection of particle pairs

It is a fundamental feature of MMC that the mixing must be local. This is to model the physical behavior of a flow, where the field is continuous in space and there is a limit to the distance an eddy can transport a parcel of fluid within the duration of a computational time step. For alternative RANS implementations of MMC,[30,31,51,52] localness is enforced by mixing particles that are neighboring in reference space. An alternative approach is preferred here. Wandel[53] has shown that if the product $n_p\Delta t$ (where n_p is the total number of particles to be mixed) is too small, then the transport of ξ is insufficient to reorder the particles. The consequence is that the particles will reach the mean value of the pair, which results in the cessation of mixing despite the significant value of N. Even if $n_p\Delta t$ is sufficiently large to avoid particles mixing exclusively with another particle, the outcome of the mixing process is not independent of $n_p\Delta t$ until $n_p\Delta t$ becomes sufficiently large that $\Delta\xi^{*p}$ guarantees that particles will change their order.

The current approach follows Wandel[39] and specifies that particle q can only mix with particle p if it is closer than some length scale $\mathcal{L}$:

$$|\xi^{*p} - \xi^{*q}| \leq \mathcal{L}. \tag{36}$$

The particle pair is randomly selected from the pool of particles that satisfy Eq. (36) and have not mixed within that time step; no further bias is imposed. Equation (36) causes the model to be independent of $n_p\Delta t$ for relatively low values of $n_p\Delta t$. However, if $\mathcal{L}$ is too large, then the localness of the model is lost.

To determine $\mathcal{L}$, it has been suggested[39] that the turbulent diffusion length scale based on B, the turbulent diffusivity of ξ, be used:

$$\mathcal{L} \equiv \sqrt{B\Delta t}. \tag{37}$$

This length scale is used here as it is expected that particles move in ξ-space by $\mathcal{L}$ every time step. Therefore, during the interval Δt, the parcels of fluid represented by the stochastic particles p and q have been sufficiently close for sufficiently long enough to interact, (i.e., mix). The impact of $\mathcal{L}$ on BLM-MMC is studied in Sec. III E.

For compliance with the mapping function $\langle Z|\xi\rangle = X(\xi)$, the following relationship between the dissipation rates is required:

$$\langle B\rangle \equiv \langle N\rangle \left\langle \left(\frac{\partial Z}{\partial \xi}\right)^2 \right\rangle^{-1}, \tag{38}$$

where $\langle N\rangle$ is obtained from Eq. (5). This formula is closed by modeling the derivative as $\partial Z/\partial\xi \approx \partial\langle Z|\xi\rangle/\partial\xi$, then estimating it using the gradient from a series of linear least squares curve-fits through ξ-space,[39] a technique which is used in all RANS implementations of MMC. For BLM-MMC, the simplification $\partial\langle Z|\xi\rangle/\partial\xi = 1$ follows from Eq. (33). However, in the current work the derivative was calculated numerically, instead of applying this simplification, because $\langle Z|\xi\rangle \neq E(Z|\xi)$ since $Z''' \neq 0$.

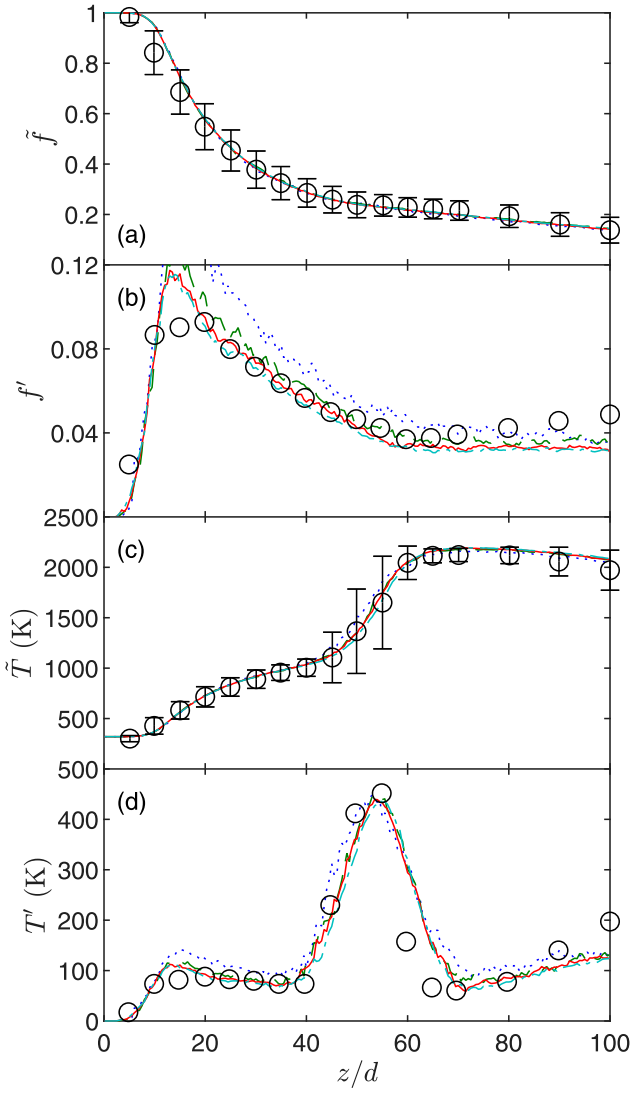

FIG. 1. Ensemble mean of centerline Favre-statistics for different numbers of particles in the simulation. (a) Mean mixture fraction; (b) mixture fraction rms; (c) mean temperature; and (d) temperature rms. BLM-MMC number of particles per cell: $n_p = 100$, · · ·; 200, – –; 400, —; 800, – ·. Experiment,[27] ◦.

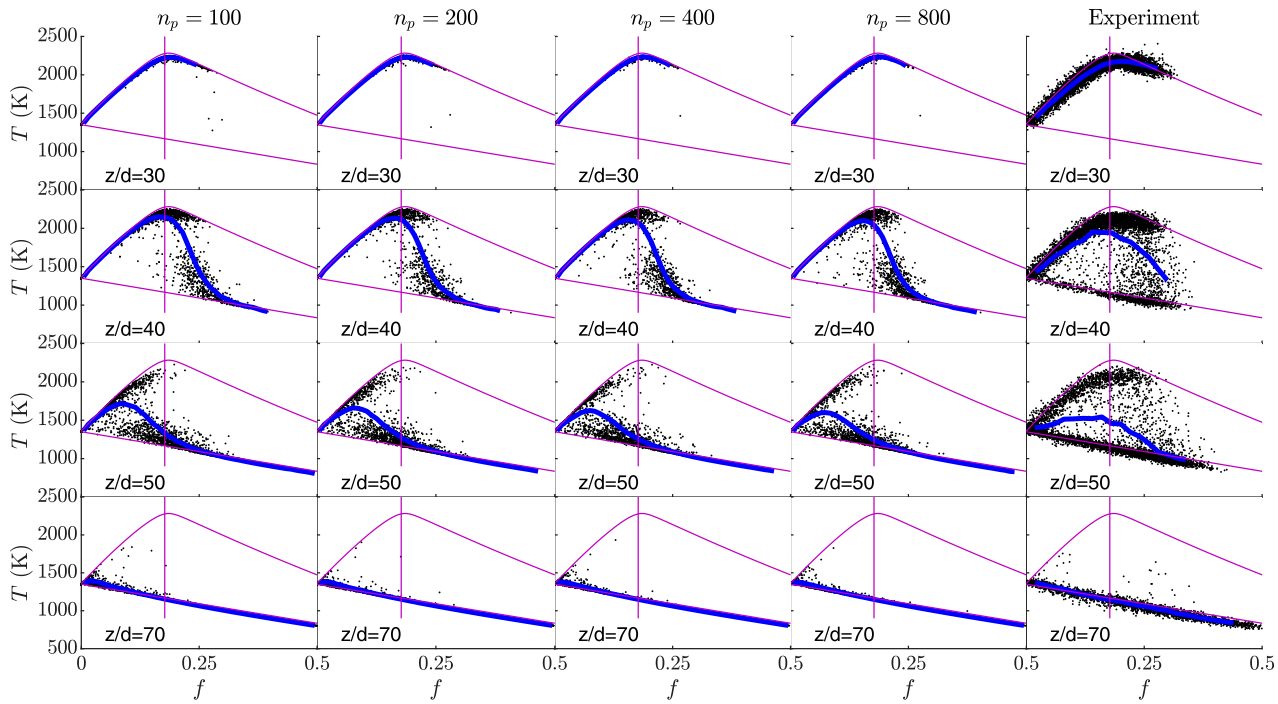

FIG. 2. Scatter plot of temperature vs mixture fraction for BLM-MMC for the cases shown in Fig. 1. There are 2500 randomly selected data points shown at various stations. Conditional temperature $\langle T|Z\rangle$: —. Equilibrium (upper) and frozen (lower) limits, and stoichiometric mixture fraction (vertical line): —.

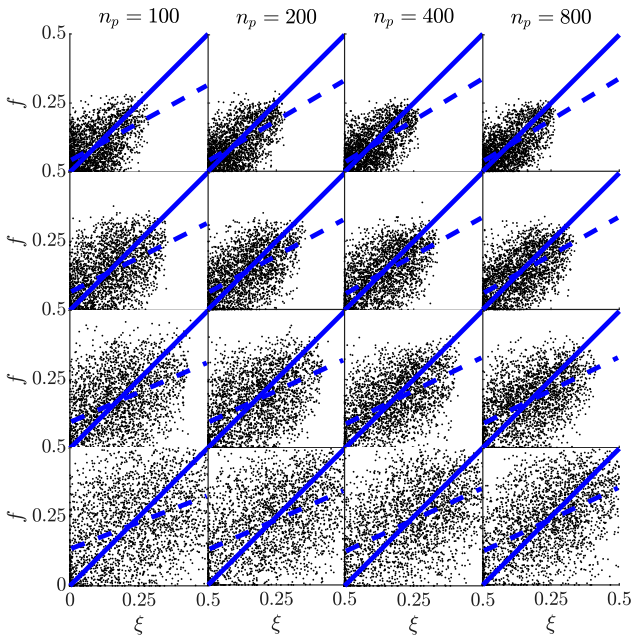

FIG. 3. Scatter plot of mixture fraction vs reference variable for BLM-MMC. The values of n_p and stations align with Fig. 2. There are 2500 randomly selected data points. Theoretical —; linear least squares curve fit – –.

III EFFECT OF INDEPENDENT PARAMETERS

In this section, the sensitivity of BLM-MMC to the independent parameters is explored, preceded by a description of the experimental case used for the study (Sec. III A). Numerical details that were kept the same throughout the simulations and evidence of numerical convergence are provided. The chemistry was solved using direct integration with the applied systematically reduced chemical mechanism featuring 48 species (28 in steady-state) and 300 reactions.[20]

A. Test case

The experimental case used for the parametric study is a methane-air jet[27] containing CH_4 33% v.v., with a velocity of 100 m/s

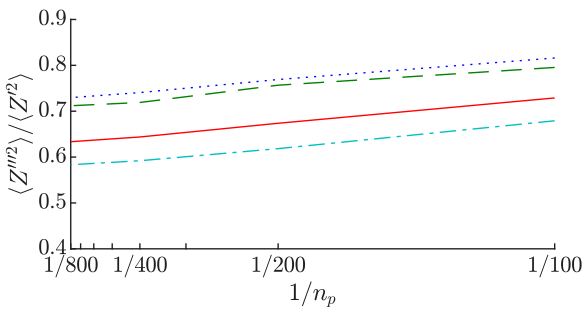

FIG. 4. Normalized scatter Eq. (13) for different numbers of particles. The lines represent different stations: $z/d = 30$, · · ·; 40, – –; 50, —; 70, – ·.

and pipe diameter of 4.57 mm, producing a jet Reynolds number Re = 28, 000; the fuel stream was at room temperature. The coflow was vitiated air with a lean mixture of H_2 at an equivalence ratio of 0.4; this mixture was completely burned upstream of the coflow region, and flowed at 5.4 m/s at a temperature of 1350 K. Because ignition of the jet necessitates sufficient mixing with the coflow to have a combustible mixture above the autoignition temperature, this configuration produces a lifted flame. As autoignition is dependent on the turbulent mixing, the flame liftoff height is very sensitive to both the fluid mechanics and the chemistry of the system. Accordingly, the ability to accurately model local extinction/reignition behavior is critical to correctly predict the behavior of this flame.

This experiment[27] produces a relatively short jet core (approximately 5 jet diameters long) before the centerline starts to be influenced by the coflow, with a sudden jump in the mixture fraction rms that starts to decay after 20 jet diameters and continues decaying until after the flame. The mean temperature experiences a reasonably steady rise (the rate diminishes once the mixture fraction rms starts to decay) until the large increase through the flame front (which occupies the region approximately 40–60 jet diameters downstream of the jet exit), followed by a steady value. The temperature rms has a sudden rise that mirrors the mixture fraction rms rise, then remains relatively constant until rapidly rising at the start of the flame front, with a large peak in the middle of the flame front and a decay back to the pre-flame levels at the end of the flame front. Models typically can predict the mixture fraction statistics and the centerline mean temperature reasonably well, but predicting the locations of the rise and/or fall of the centerline temperature rms within the flame front is very challenging.

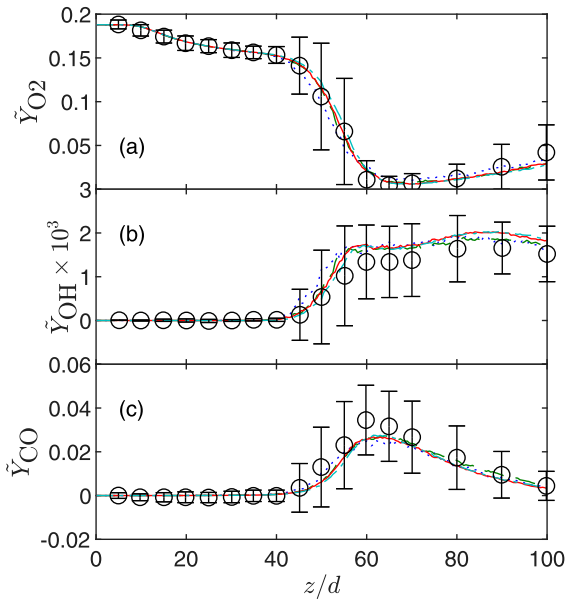

FIG. 5. Ensemble mean of centerline Favre-averaged mass fraction for the cases shown in Fig. 1. (a) Molecular oxygen (O_2); (b) hydroxyl radical (OH); and (c) carbon monoxide (CO). Lines: BLM-MMC; experiment,[27] – °.

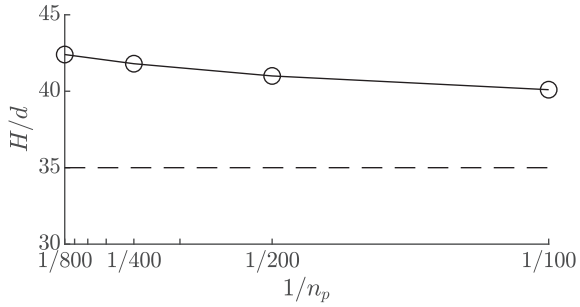

FIG. 6. Liftoff height of flame for variations in n_p. BLM-MMC, —; Experiment[27] $H/d = 35$.

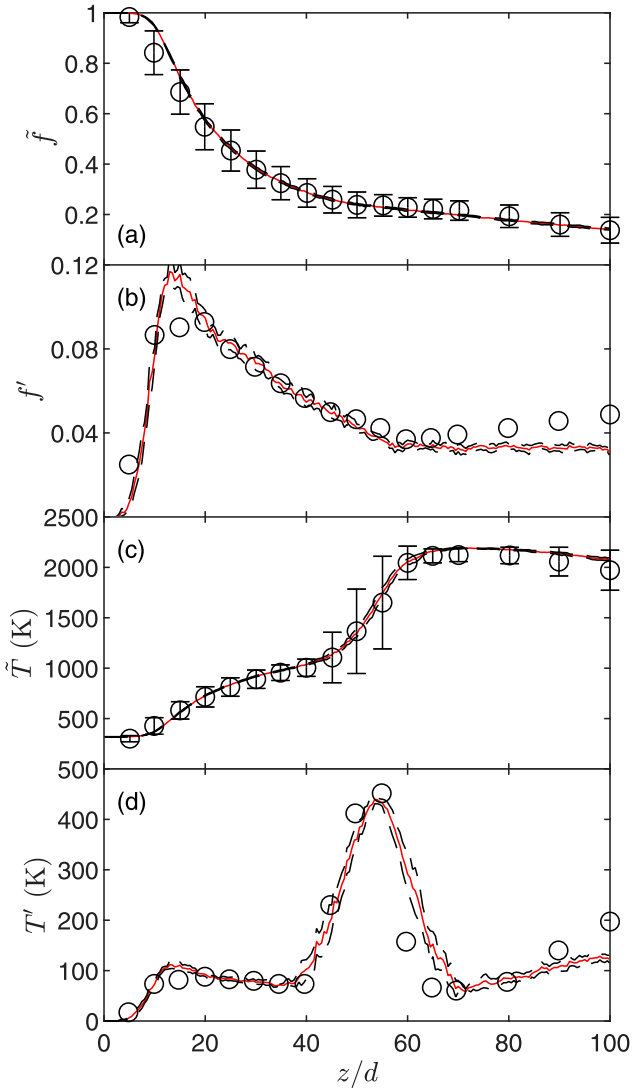

FIG. 7. Confidence interval for $n_p = 400$ particles per cell. (a) Mean mixture fraction; (b) mixture fraction rms; (c) mean temperature; and (d) temperature rms. BLM-MMC: ensemble mean, —; 95% confidence interval, – –. Experiment,[27] °.

The computer code used to solve the case uses a parabolic implementation and has been successfully used previously[33,54] to simulate the experimental case. The axisymmetric domain was discretized using 80 cells in the radial direction, with a concentration of cells in the region of the jet core, and the width of the domain increasing with downstream distance. On average, there were 400 particles per cell with an ensemble of 10 simulations.

B. Base case numerical settings and convergence

The base case numerical settings (identified to be optimal) are defined in Table I, and this configuration is shown as a solid red line, in all figures for ease of comparison.

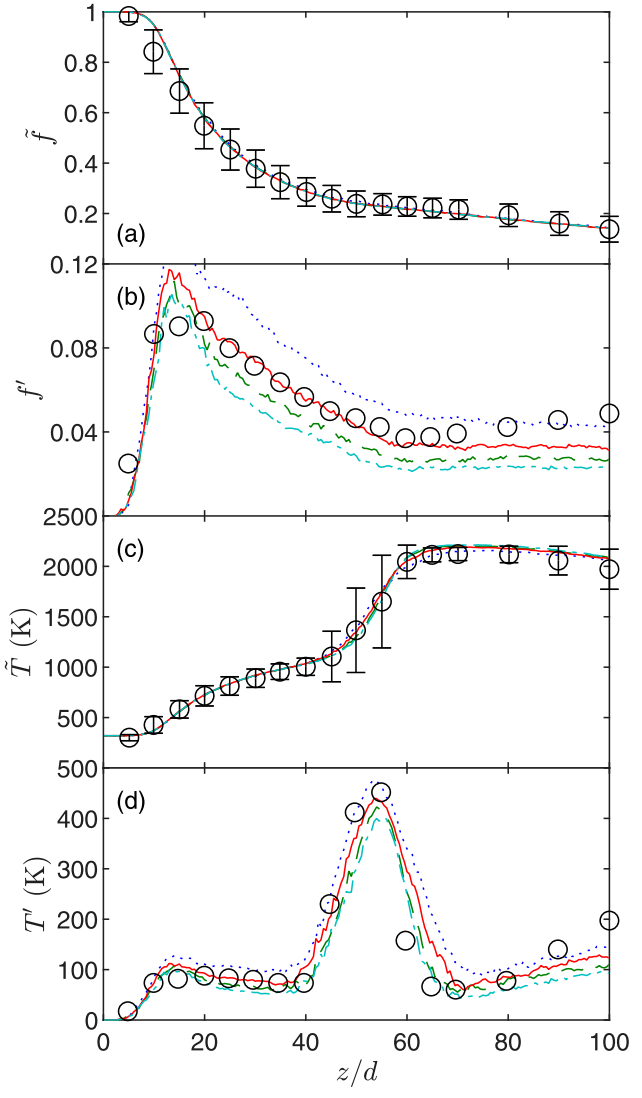

FIG. 8. Ensemble mean of centerline Favre-statistics for different values of C_Z. (a) Mean mixture fraction; (b) mixture fraction rms; (c) mean temperature; and (d) temperature rms. BLM-MMC: $C_Z = 0.75$, · · ·; 1.0, —; 1.25, – –; 1.5, – ·. Experiment,[27] ◦.

TABLE I. Parameters identified as optimal for $P_\alpha(\alpha) = \delta(\alpha - \alpha_0)$ and 400 particles per cell. These parameters are defined to be the "base settings." The number of simulations in the ensemble for each case is n_e.

Parameter	C_Z	α_0	$\mathcal{L}$	$\mathcal{P}_m$	n_e
Value	1.0	0.5	$\sqrt{B\Delta t}$	0.07	10

To verify numerical convergence of the base case settings, the effect of the number of particles per cell was tested, by comparing 100, 200, 400, and 800 particles per cell. The centerline Favre-averaged results (Fig. 1) show that there is significant variation in results for $n_p = 100$ particles per cell. Larger numbers produce similar results with 400 and 800 particles per cell showing little difference. This behavior is caused by a bias introduced by the rapid burning of particles that are close to stoichiometry for smaller sample sizes (Fig. 2).

The mapping of the mixture fraction f to the reference variable ξ governs the entire mixing process, and is shown in Fig. 3. The scatter, which is measured using Eq. (13), is close to fully converged for 400 particles per cell (Fig. 4).

Considering the mass fraction of species in Fig. 5, the inverse of O_2 has the same behavior as the mean temperature. The behavior of OH is similar to the mean temperature except for not significantly changing prior to the flame front and some production far downstream; CO is similarly not produced in significant quantities

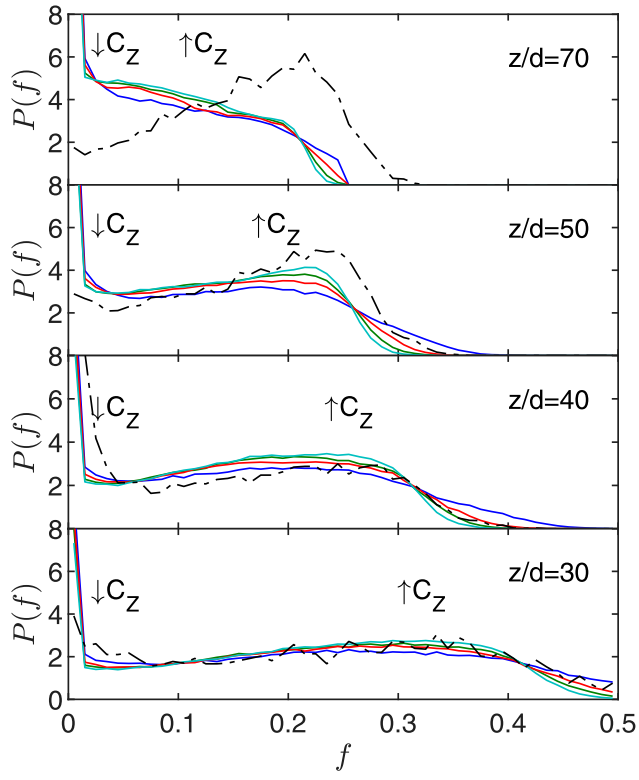

FIG. 9. Mixture fraction PDFs at various stations for C_Z in Fig. 8. Lines: BLM-MMC; Experiment,[27] – ·. The arrow indicates the direction of increasing C_Z.

upstream of the flame front, but is almost completely consumed by the end of the domain. The sensitivity of the species to the number of particles is similar to the mean temperature.

The flame liftoff height is calculated[27] by taking the ensemble average of the axial locations where the centerline mean mole fraction of C_2H_4 reached 100 ppm and C_2H_2 reached 2 ppm. Increasing the number of particles slightly increased the liftoff height toward an asymptote (Fig. 6), indicating that the system is close to convergence. While the computed liftoff height of $H/d \simeq 42$ is higher than the experimental value of 35, Cao *et al.*[55] showed that the liftoff height is exceptionally sensitive to initial temperature of the coflow with a decrease in 10 K doubling the value of H/d. Hence, no attempt was made to reduce the discrepancy. For 400 particles per cell, the location of the threshold value of C_2H_4 varied by $\pm 1.5\, z/d$ within the ensemble, while the location varied by $\pm 4\, z/d$ for C_2H_2; therefore, stochastic variability is not a principal concern.

To numerically verify convergence, calculations were made for each number of particles to determine the confidence interval:

$$\mathrm{CI} \equiv \bar{x} \pm ts/\sqrt{n_e}, \tag{39}$$

where $\bar{x}$ is the ensemble mean, t is the chosen Student's t-value, s is the ensemble standard deviation, and n_e is the number of simulations in the ensemble. A confidence level of 95% was chosen; as there were 10 simulations per ensemble, there are 9 degrees of freedom; therefore, the two-sided Student's t-value is 2.262. The confidence interval is shown for 400 particles per cell in Fig. 7, where the results for $n_p = 800$ lie within the 95% confidence interval; therefore, convergence has been verified. As a consequence, $n_p = 400$ particles per cell will be used in the remainder of this paper.

It should be noted that the results presented in Fig. 7 represent the best match to the experimental data of any simulation that has been published, including LES and RANS.[33] The improvement over previous results using BLM–MMC[33] is due to the selection of C_Z, which has been decreased from 2.0 to 1.0.

C. Effect of turbulent-scalar timescale ratio, C_Z

The primary variable that needs to be considered is C_Z because it is a macro-parameter that is common for all turbulent combustion models. Because it is defined to control the dissipation rate of the unconditional fluctuations of mixture fraction, Eq. (4), the standard deviation should monotonically decrease as C_Z increases (with all other parameters fixed, as per Table I). This is shown to be the case throughout the domain for both mixture fraction and temperature in Fig. 8, where increasing C_Z causes a translation downwards. There is no significant effect on the mean mixture fraction, Fig. 8(a), of varying C_Z (or any of the other parameters). However, there is a small but significant effect on the mean temperature, Fig. 8(c), of increasing C_Z: a slight decrease in the flame thickness (i.e., a greater rate of increase through the flame), with the center of the flame approximately in the same location. This behavior is mirrored in the temperature rms, Fig. 8(d).

The mixture fraction PDF (Fig. 9) is a key indicator of the performance of the model because the distributions of mixture fraction control every aspect of non-premixed combustion. In general, the model predicts the experimental behavior very well for the upstream locations, with discrepancies in the downstream locations. It can be concluded that BLM-MMC produces one of the desired outcomes of

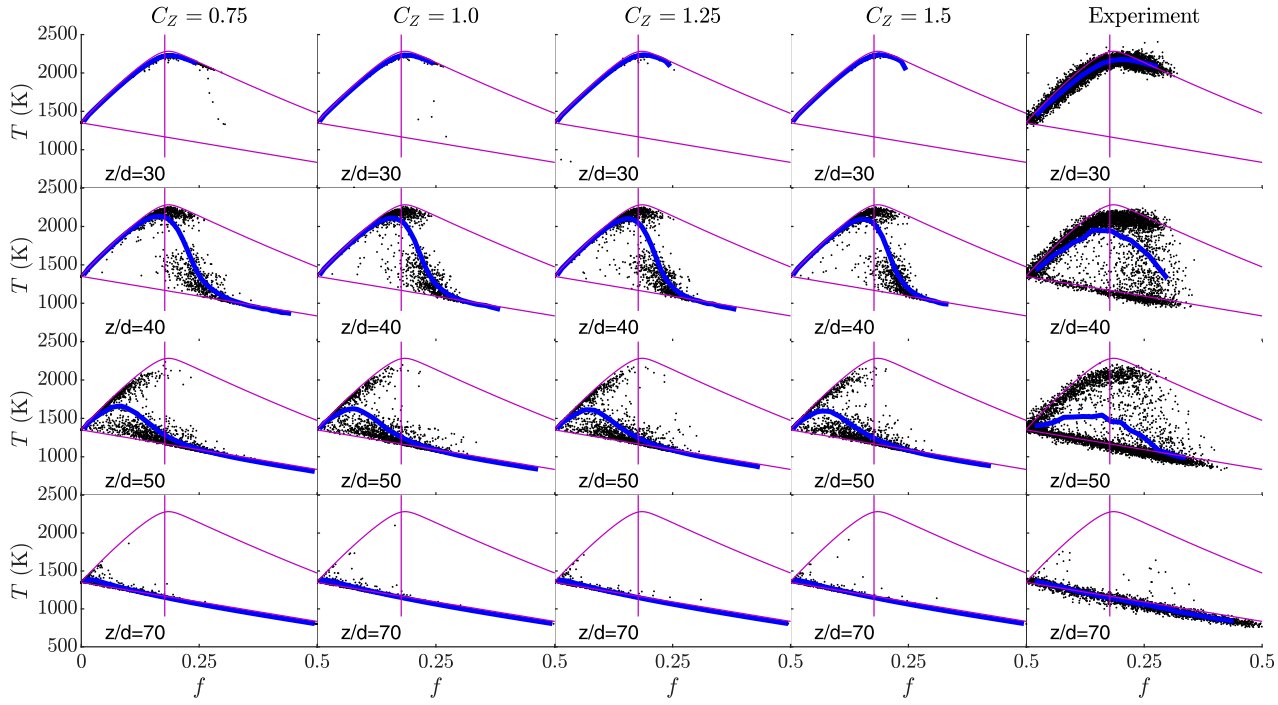

FIG. 10. Scatter plot of temperature vs mixture fraction for BLM-MMC. Each column has the same values of C_Z as shown in Fig. 8. There are 2500 randomly selected data points shown at various stations. Conditional temperature $\langle T|Z\rangle$: —. Equilibrium (upper) and frozen (lower) limits, and stoichiometric mixture fraction (vertical line): —.

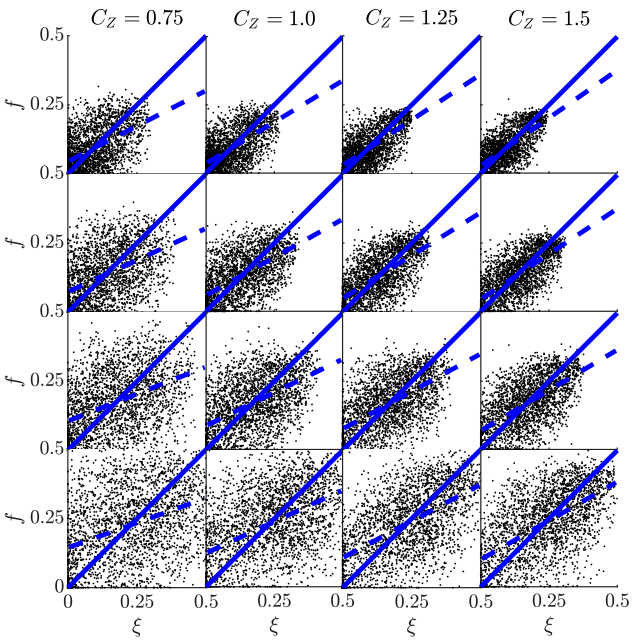

FIG. 11. Scatter plot of mixture fraction vs reference variable for BLM-MMC. The values of C_Z and stations align with Fig. 10. There are 2500 randomly selected data points. Theoretical —; linear least squares curve fit – –.

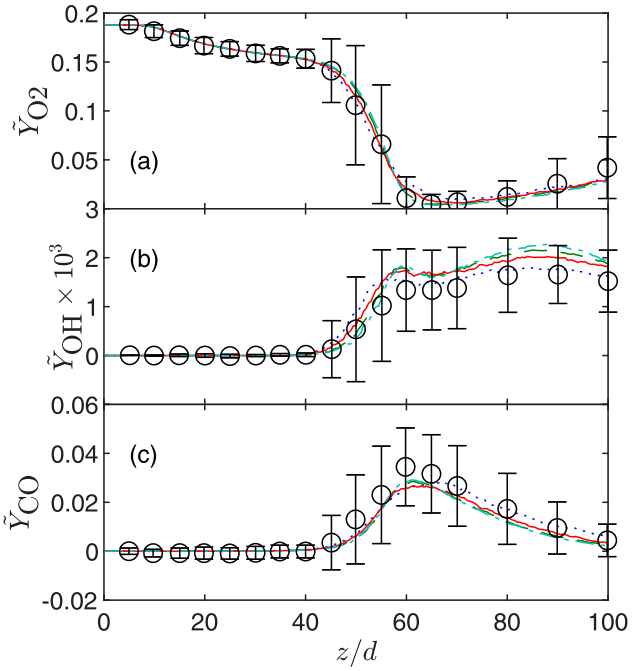

FIG. 13. Ensemble mean of centerline Favre-averaged mass fraction for C_Z in Fig. 8. (a) Molecular oxygen (O_2); (b) hydroxyl radical (OH); and (c) carbon monoxide (CO). Lines: BLM-MMC; Experiment,[27] – ◦.

MMC of providing a viable, accurate model for $P_Z(Z)$. For increasing C_Z, it is unsurprising that the maximum possible value decreases, since those extreme values are mixed more intensely toward the mean. Because the width of the PDF narrows with increasing C_Z, the local maxima away from the coflow (i.e., located at $f > 0$) becomes larger, but the general shape is preserved.

Because the principal effect of C_Z is on the mixture fraction rms, there is little impact on the relationship between temperature and mixture fraction (Fig. 10). The only noticeable variation is that the highest value of mixture fraction along the frozen line decreases with increasing C_Z due to the more intense mixing (as indicated by the PDFs in Fig. 9).

Increasing C_Z increases the mixing intensity, thereby increasing the correlation between the mixture fraction f and reference variable ξ (Fig. 11). Meanwhile, the scatter slowly decreases with distance downstream, Fig. 12(a), because the mixture fraction distribution becomes narrower (Fig. 9). Note that Fig. 12 shows the data for the timescale ratio between the conditional fluctuations and unconditional fluctuations, Eq. (13), and is much larger than the value of 1/8 originally proposed[38] and used as the standard value in most MMC simulations. Instead, the timescale ratio needs to decay with distance downstream, which is in agreement with the theory proposed by Wandel[39] that the timescale ratio should not be a constant.

The effect of C_Z on the species (Fig. 13) is similar to the effect of the number of particles (c.f. Fig. 5), although when $C_Z < 1$ the species mass fractions are more sensitive to C_Z. The liftoff height is largely insensitive to C_Z, Fig. 14(a), because C_Z only significantly affects the mixture fraction rms.

D. Effect of Modified Curl's mixing amount, $\langle\alpha\rangle$

The mixing amount α, defined in Sec. II D, is the amount that two particles mix, ranging from 0 representing no mixing to 1 representing complete mixing. A δ-function PDF for $P_\alpha(\alpha)$ (with $\langle\alpha\rangle = \alpha_0$) is tested for different values of α_0; these are compared with a uniform distribution for α, with $\langle\alpha\rangle = 0.5$ directly compared with $\alpha_0 = 0.5$. All other parameters were fixed according to Table I.

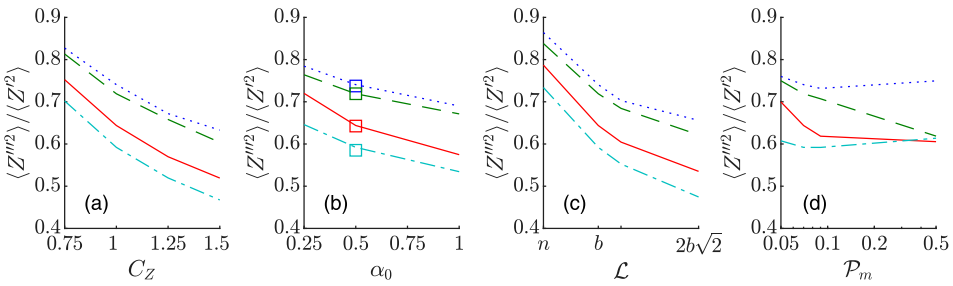

FIG. 12. Normalized scatter Eq. (13) for different parameters of BLM-MMC. (a) C_Z; (b) α where □ shows uniform random for P_α; (c) $\mathcal{L}$ where $n =$ neighbor and $b = \sqrt{B\Delta t}$; (d) $\mathcal{P}_m$. The lines represent different stations: $z/d = 30$, · · ·; 40, – –; 50, —; 70, – ·.

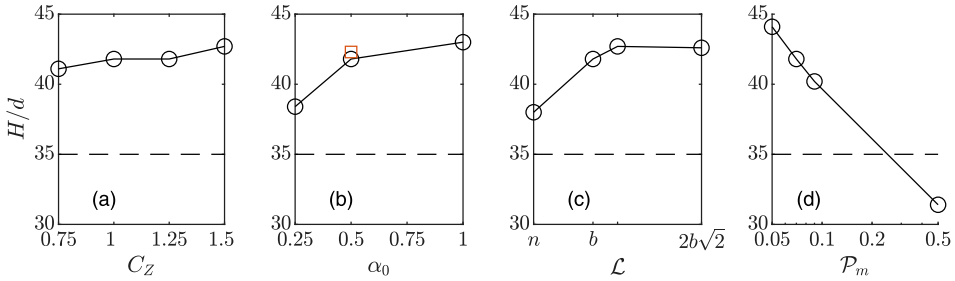

FIG. 14. Comparison of liftoff heights for different parameters of BLM-MMC. The dashed line represents the experimental value.[27] (a) C_Z; (b) α where □ shows uniform random for P_α; (c) $\mathcal{L}$ where n = neighbor and $b = \sqrt{B\Delta t}$; (d) $\mathcal{P}_m$.

As expected, the mean mixture fraction is not influenced by this parameter, Fig. 15(a). Increasing $\langle\alpha\rangle$ decreases the peak value of the mixture fraction rms, Fig. 15(b); however, this is not a global effect, since the values converge downstream of the flame front. As a consequence, the mixture fraction PDFs are almost identical for the stations considered. Although the flame front commences at approximately the same location, Fig. 15(c), the flame narrows with increasing $\langle\alpha\rangle$ because the intensity of mixing is increased; hence, cold particles are more likely to become warmer than the autoignition temperature after mixing. The temperature rms, Fig. 15(d), behaves similarly to both the mixture fraction rms (with the same impact on the initial peak value followed by convergence) and the mean temperature (with a slight delay to the flame front commencement, but a significant decrease in flame thickness with increasing $\langle\alpha\rangle$).

The effect of $P_\alpha(\alpha)$ is relatively minor. The uniform distribution causes a slight increase in the peak value of mixture fraction rms, and a marginal decrease downstream, while it produces a slight delay to the flame front commencement with a corresponding decrease in flame thickness (the end of the flame front is only marginally delayed). It seems that the particles which mix by a smaller amount have a slightly greater influence on the results than those particles which mix by a greater (equivalent) amount.

The impact of $\langle\alpha\rangle$ on the temperature distribution is clearly seen in Fig. 16. At low values of $\langle\alpha\rangle$, the frozen and equilibrium particles are essentially segregated for the duration of the simulation, so the frozen particles slowly warm as a group toward the autoignition temperature. In other words, for low values of $\langle\alpha\rangle$, no local extinction/reignition occurs. In contrast, at high values of $\langle\alpha\rangle$, there is excessive extinction/reignition, as the extinguishing particles cause frozen particles to quickly reach the autoignition temperature. This creates a continuum of temperatures for a given mixture fraction, as all the fluid progresses to equilibrium. At the intermediate value of mixing ($\langle\alpha\rangle = 0.5$), there is some extinction, but those extinguishing particles quickly reignite, while the frozen particles are strongly drawn toward the autoignition temperature. The influence of $P_\alpha(\alpha)$ is mostly for lean mixtures, where there is more segregation of the particles in frozen and equilibrium states for the uniform distribution. At $z/d = 40$, the δ-function produces more of a continuum of temperatures, while at $z/d = 50$, it leaves very few particles below the autoignition temperature.

The mapping from the MMC reference variable ξ to the mixture fraction f for the different amounts of mixing is shown in Fig. 17. Figure 12(b) shows that there is a decrease in scatter with increase in $\langle\alpha\rangle$, while the distribution of P_α has negligible impact. This is because the increase in the average intensity of each mixing event causes particles to approach a more similar value of mixture fraction.

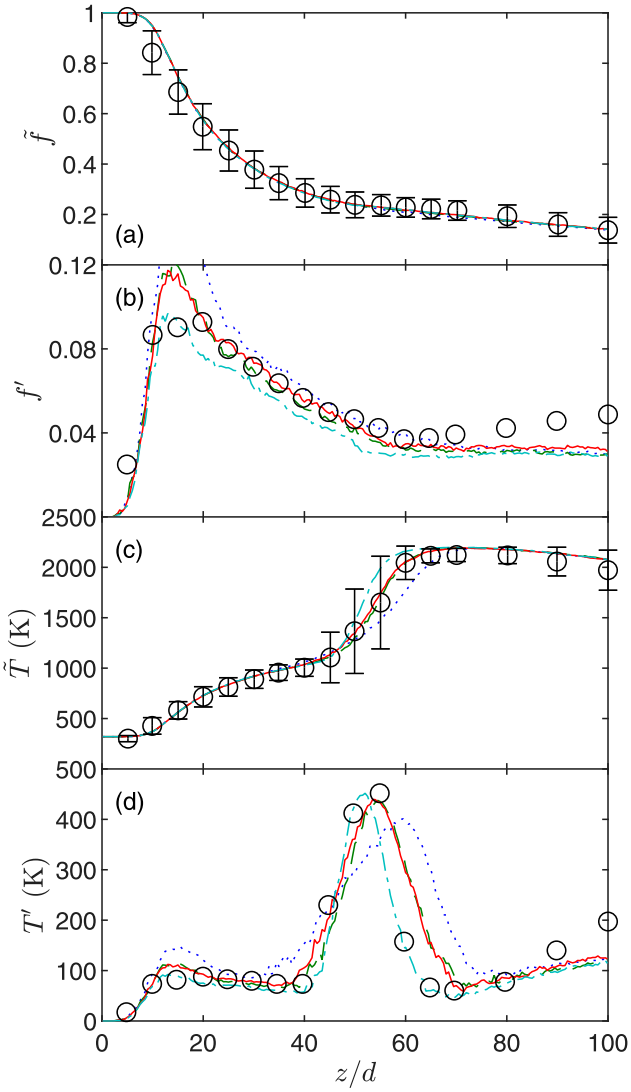

FIG. 15. Ensemble mean of centerline Favre-statistics for different amounts of mixing. (a) Mean mixture fraction; (b) mixture fraction rms; (c) mean temperature; (d) temperature rms. BLM-MMC: $\alpha_0 = 0.25$, ···; uniform random number ($\langle\alpha\rangle = 0.5$), – –; $\alpha_0 = 0.5$, —; 1.0, – ·. Experiment,[27] ∘.

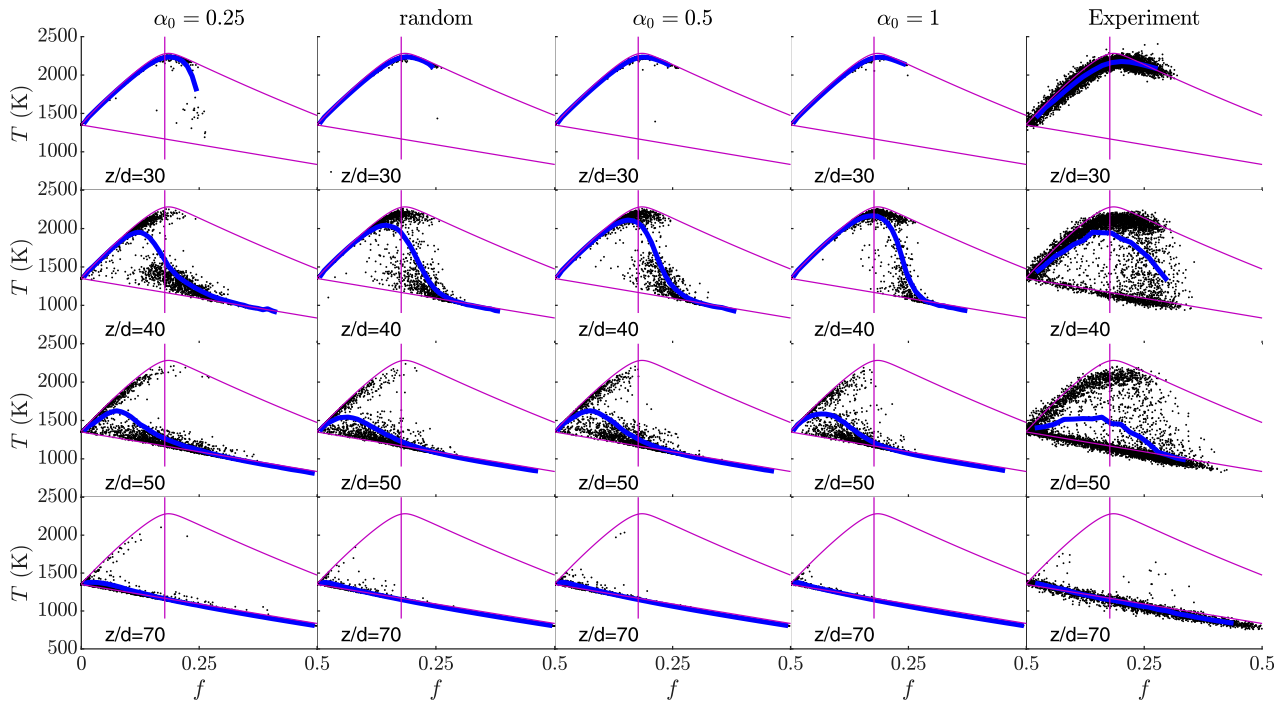

FIG. 16. Scatter plot of temperature vs mixture fraction for BLM-MMC. Each column has the same values of $\langle\alpha\rangle$ as Fig. 15. There are 2500 randomly selected data points shown at various stations. Conditional temperature $\langle T|Z\rangle$: —. Equilibrium (upper) and frozen (lower) limits, and stoichiometric mixture fraction (vertical line): —.

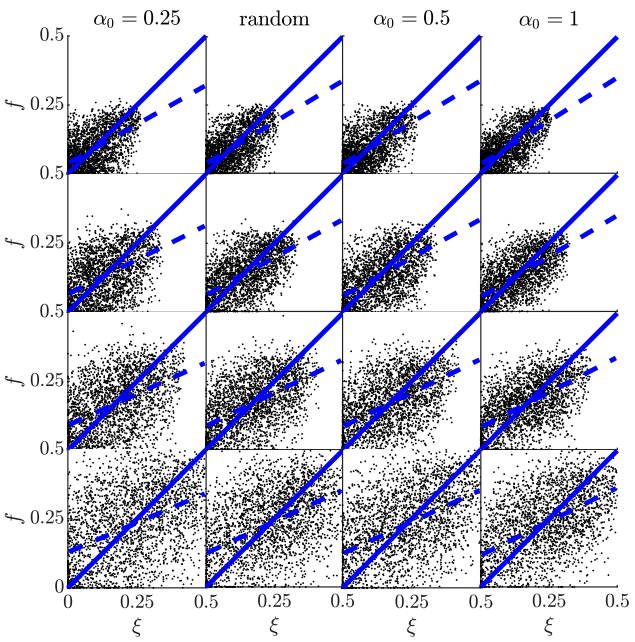

FIG. 17. Scatter plot of mixture fraction vs reference variable for BLM-MMC. The values of α and stations align with Fig. 16. There are 2500 randomly selected data points. Theoretical —; Linear least squares curve fit – –.

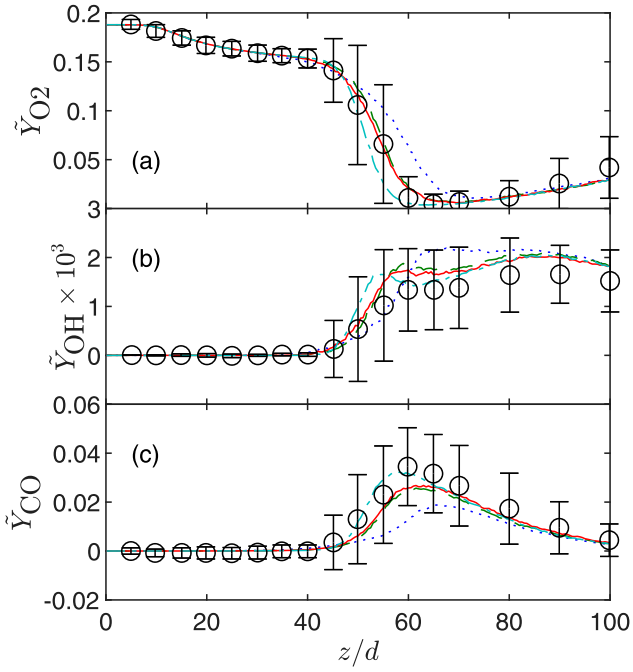

FIG. 18. Ensemble mean of centerline Favre-averaged mass fraction for the different mixing amounts α in Fig. 15. (a) Molecular oxygen (O_2); (b) hydroxyl radical (OH); and (c) carbon monoxide (CO). Lines: BLM-MMC; Experiment,[27] – °.

The mass fractions of species (Fig. 18) show a wider band of variation for the range of parameter values considered than discussed above. The species O_2, OH, and CO are sensitive within the flame region. A low α leads to underpredictions of CO and OH. The liftoff height, Fig. 14(b), is largely insensitive to the mixing amount for $\langle\alpha\rangle \geq 0.5$, but becomes more sensitive for small values of $\langle\alpha\rangle$.

E. Effect of the mixing distance, $\mathcal{L}$

Maintaining locality of mixing is fundamental to accurately predict local extinction/reignition. Four different limits $\mathcal{L}$, Eq. (36), were applied to restrict the availability of particles for pairing: the "neighbour" (i.e., the particle closest in reference space), and three distances based on the diffusion length scale; all other values were fixed according to Table I.

Figure 19 shows that the effect of increasing $\mathcal{L}$ is broadly similar to increasing C_Z: it causes a global decrease in the rms of both mixture fraction and temperature. However, this is not consistent across the whole domain. Choosing the neighbor causes the start of the flame front to advance significantly, Figs. 19(c) and 19(d), with an equal amount of stretching of the flame, since the downstream edge of the flame remains approximately the same. Considering the different distances based on the diffusion length scale, the peak value of mixture fraction rms, Fig. 19(b), is less sensitive to $\mathcal{L}$ than C_Z, while the flame front recedes slightly more with increasing $\mathcal{L}$ than the end of the flame advances. The inevitable consequence of the large variations in mixture fraction rms is that the effect on the mixture fraction PDF (Fig. 20) is similar to C_Z. As $\mathcal{L}$ increases, the maximum possible value of mixture fraction decreases, with the selection of the neighbor typically significantly over-predicting this value, and thereby flattening the PDF so that there is no discernible local maxima away from the coflow.

The impact of the mixing distance on the temperature is mostly for lean mixtures (Fig. 21), where increasing $\mathcal{L}$ decreases the rate at which particles reach the autoignition temperature. This is because particles can interact with particles whose composition is more different, so they are more likely to mix to a composition which is below the autoignition temperature for that new (more different) mixture fraction.

Increasing the range of values of ξ that are available for mixing (thereby increasing the pool of particles available for mixing)

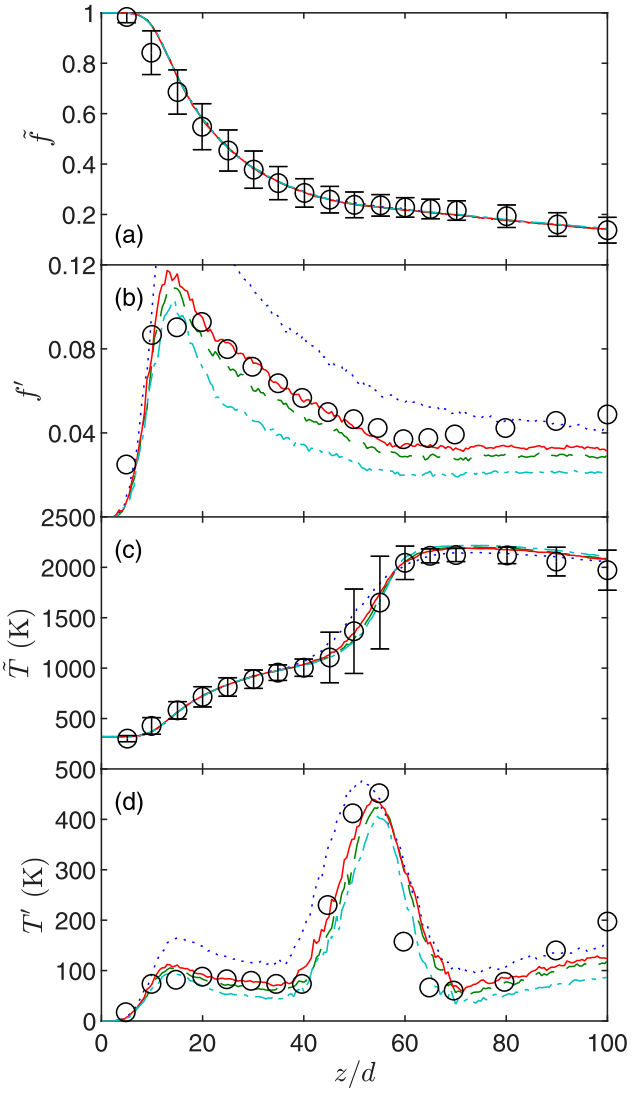

FIG. 19. Ensemble mean of centerline Favre-statistics for different mixing distances $\mathcal{L}$. (a) Mean mixture fraction; (b) mixture fraction rms; (c) mean temperature; and (d) temperature rms. BLM-MMC: $\mathcal{L}$ = neighbor, $\cdots$; $\sqrt{B\Delta t}$, —; $\sqrt{2B\Delta t}$, – –; $2\sqrt{2B\Delta t}$, – ·. Experiment,[27] ∘.

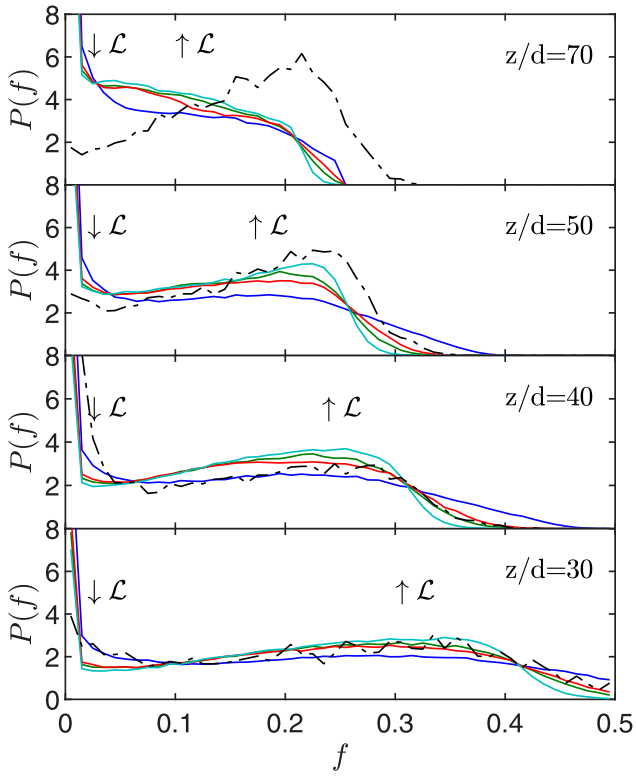

FIG. 20. Mixture fraction PDFs at various stations for values of $\mathcal{L}$ in Fig. 19. Lines: BLM-MMC; Experiment,[27] – ·. The arrow indicates the direction of increasing $\mathcal{L}$.

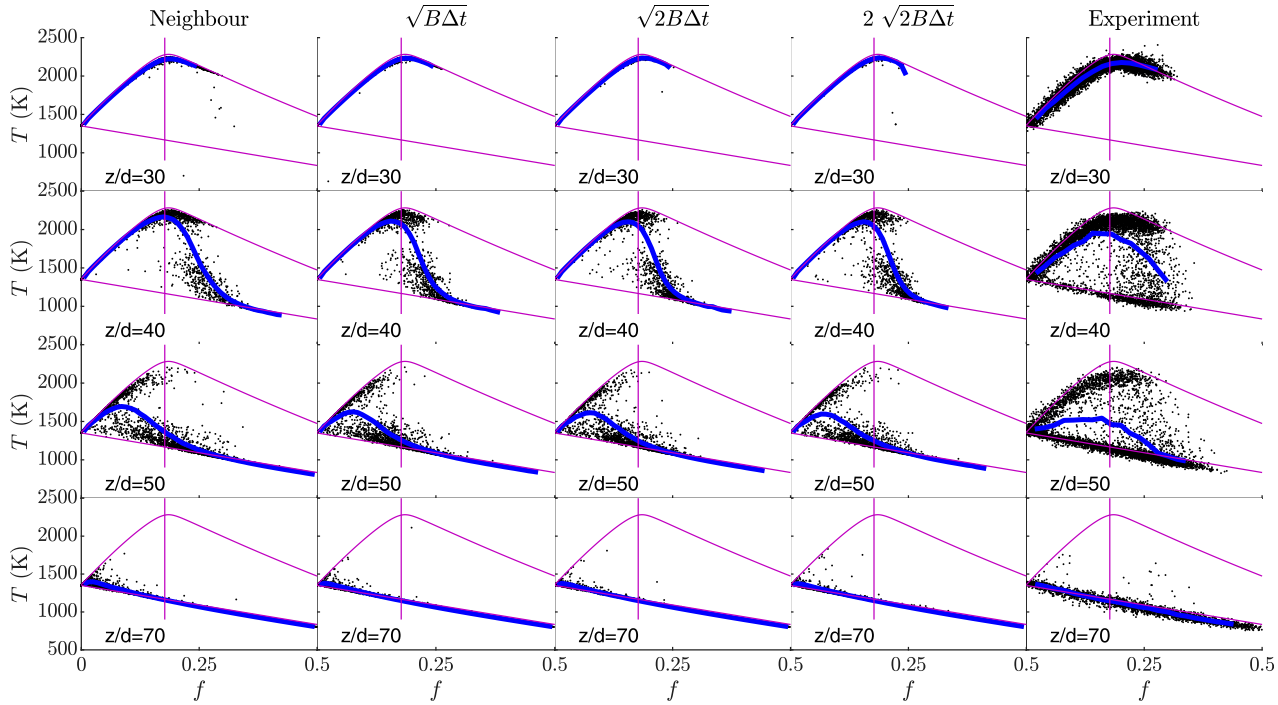

FIG. 21. Scatter plot of temperature vs mixture fraction for BLM-MMC. Each column has the same values of $\mathcal{L}$ as Fig. 19. There are 2500 randomly selected data points shown at various stations. Conditional temperature $\langle T|Z\rangle$: —. Equilibrium (upper) and frozen (lower) limits, and stoichiometric mixture fraction (vertical line): —.

significantly decreases the scatter in the mixture fraction, Figs. 22 and 12(c). The reason why the scatter is so much higher when the immediate neighbor is selected is because the equivalent behavior to stranding in EMST occurs: particles are able to mix excessively with a small subset of particles, so there is less opportunity for the particles to change their values significantly. This process can be likened to in-breeding.

The mass fractions in Fig. 23 show similar trends to α_0 in Fig. 18 except OH is sensitive further downstream of the flame as well. Mixing particles too close together causes the reactions to start too soon because there is insufficient influence of other particles; this subsequently suppresses the secondary combustion for $z/d > 70$, which assists in consuming the CO. When the distance between particle pairs is evaluated as a function of $B\Delta t$, the liftoff height is largely insensitive to $\mathcal{L}$, Fig. 14(c), although mixing neighbors advances the flame significantly.

F. Fraction of particles mixed per time step, $\mathcal{P}_m$

The remaining parameter in the BLM-MMC model is the fraction of particles that mix each time step, defined by the probability of particles mixing, $\mathcal{P}_m$. There is consistent behavior of the model for values of $\mathcal{P}_m$ that are close to the optimal value (for this case) of 0.07 (Fig. 24); the only discrepancy for the relatively large value of 0.5 is the peak mixture fraction rms, Fig. 24(b). In general, there is a modest impact of $\mathcal{P}_m$ on the mixture fraction rms (hence also the mixture fraction PDF), with an increase in $\mathcal{P}_m$ causing lower values of mixture fraction rms upstream of the flame front and higher values of the mixture fraction rms downstream of the flame front. The value of $\mathcal{P}_m$

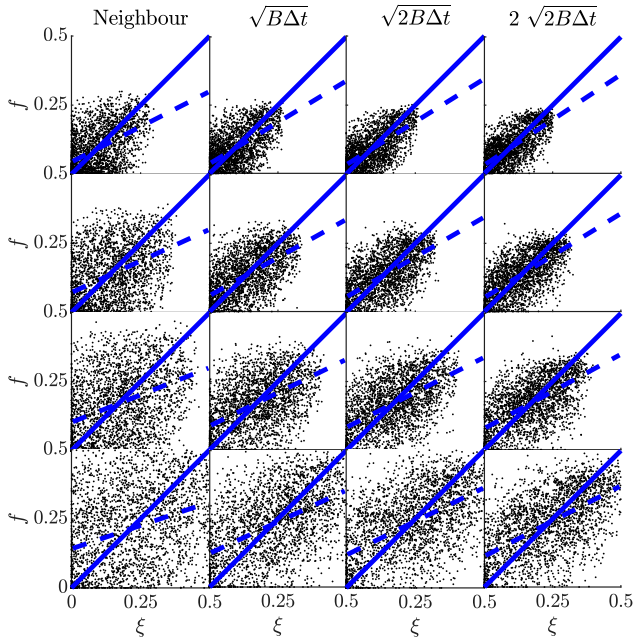

FIG. 22. Scatter plot of mixture fraction vs reference variable for BLM-MMC. The values of $\mathcal{L}$ and stations align with Fig. 21. There are 2500 randomly selected data points. Theoretical —; Linear least squares curve fit – –.

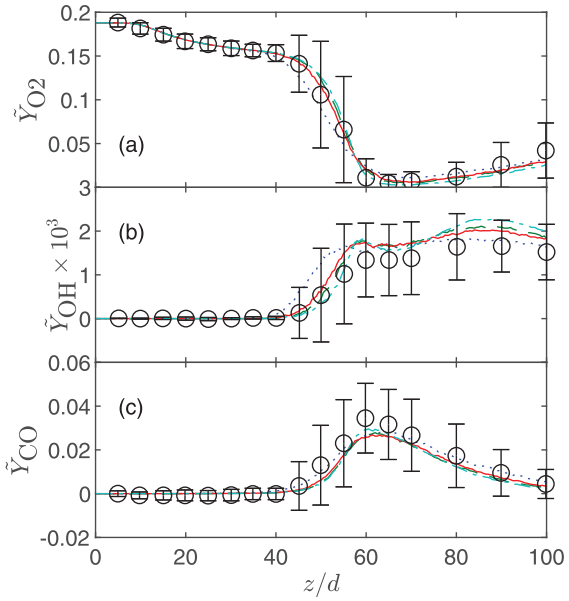

FIG. 23. Ensemble mean of centerline Favre-averaged mass fraction for the different mixing distances $\mathcal{L}$ in Fig. 19. (a) Molecular oxygen (O_2); (b) hydroxyl radical (OH); and (c) carbon monoxide (CO). Lines: BLM-MMC; Experiment,[27] – °.

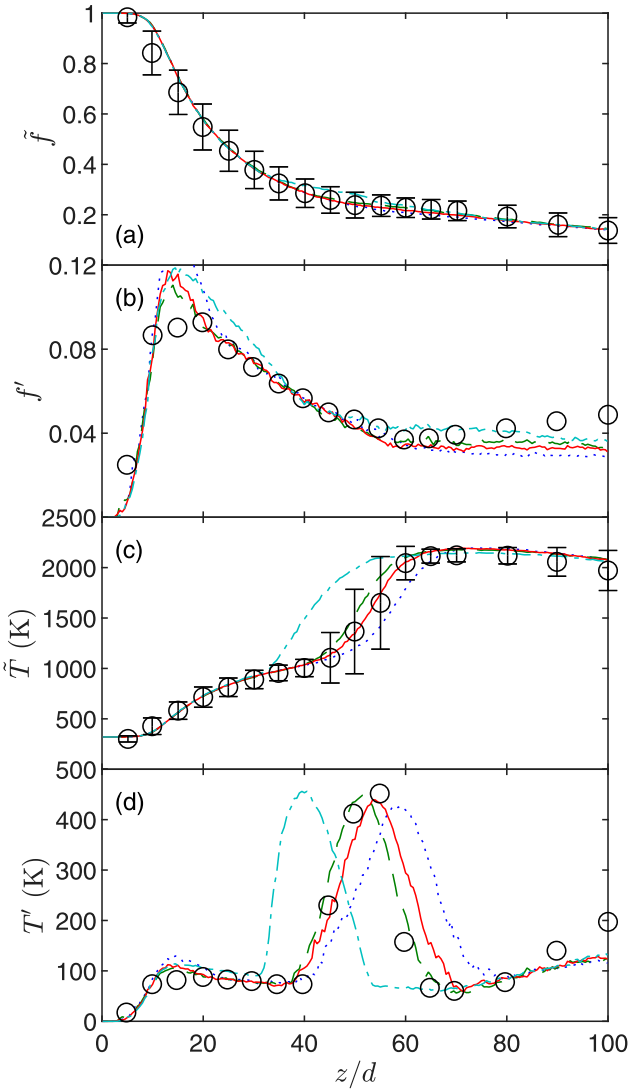

FIG. 24. Ensemble mean of centerline Favre-statistics for different fractions of particles mixing $\mathcal{P}_m$. (a) Mean mixture fraction; (b) mixture fraction rms; (c) mean temperature; and (d) temperature rms. BLM-MMC: $\mathcal{P}_m = 0.05$, · · ·; 0.07, —, 0.09, – –; 0.5, – ·. Experiment,[27] °.

does not significantly affect the flame thickness, Figs. 24(c) and 24(d), but increasing $\mathcal{P}_m$ does significantly advance the flame, while also skewing it. Besides $\mathcal{P}_m = 0.5$, the relative variations of $\mathcal{P}_m$ compared to the base case were quite significant, and comparable to the relative variations of C_Z.

The effect of increasing how many particles mix within a given time step is to increase the rate at which particles reach the autoignition temperature (Fig. 25), and also shifts the extinction/reignition events to richer mixtures. This does not significantly impact the particles close to equilibrium, except that increasing $\mathcal{P}_m$ causes particles at higher values of mixture fraction to approach equilibrium. The extreme value of $\mathcal{P}_m = 0.5$ causes all but the richest mixtures to reach equilibrium very early at $z/d = 40$. However, significant mixing still occurs downstream of this location, so some of the fuel particles remain below the autoignition temperature further downstream, even as they approach stoichiometry.

The fraction of particles mixing does not significantly influence the scatter in the mixture fraction, Figs. 26 and 12(d), because the same behavior is repeated for each particle.

The mass fractions shown in Fig. 27 have a wider range of values than previous parameters because the values of $\mathcal{P}_m$ differ by an order of magnitude. The mass fractions of O_2 and CO are very distinct compared to the lower sensitivities for the other parameters. The lowest value of $\mathcal{P}_m$ produces unique results because of the significant delay due to insufficient particles achieving a combustible mixture. Other than this difference, $\mathcal{P}_m$ behaves similarly to the other parameters. There is a clear relationship between $\mathcal{P}_m$ and liftoff height, Fig. 14(d), and the liftoff height is sensitive to this parameter.

IV. CONCLUSIONS

This paper investigated the effects of the various free parameters within the generalized binomial Langevin–multiple mapping conditioning model using the binomial Langevin mixture fraction as the reference variable for MMC (BLM-MMC). The sensitivity of the model was tested using a lifted flame that displays significant local extinction/reignition behavior. Recommendations for how the parameters should be specified follow. The model for the dissipation rate of the mixture fraction (C_Z) should be specified first, and should take the standard value[46] of 1.0; this model only significantly impacts the mixture fraction rms by causing a global decrease as C_Z increases, with the temperature rms affected in the same manner, but with reduced sensitivity.

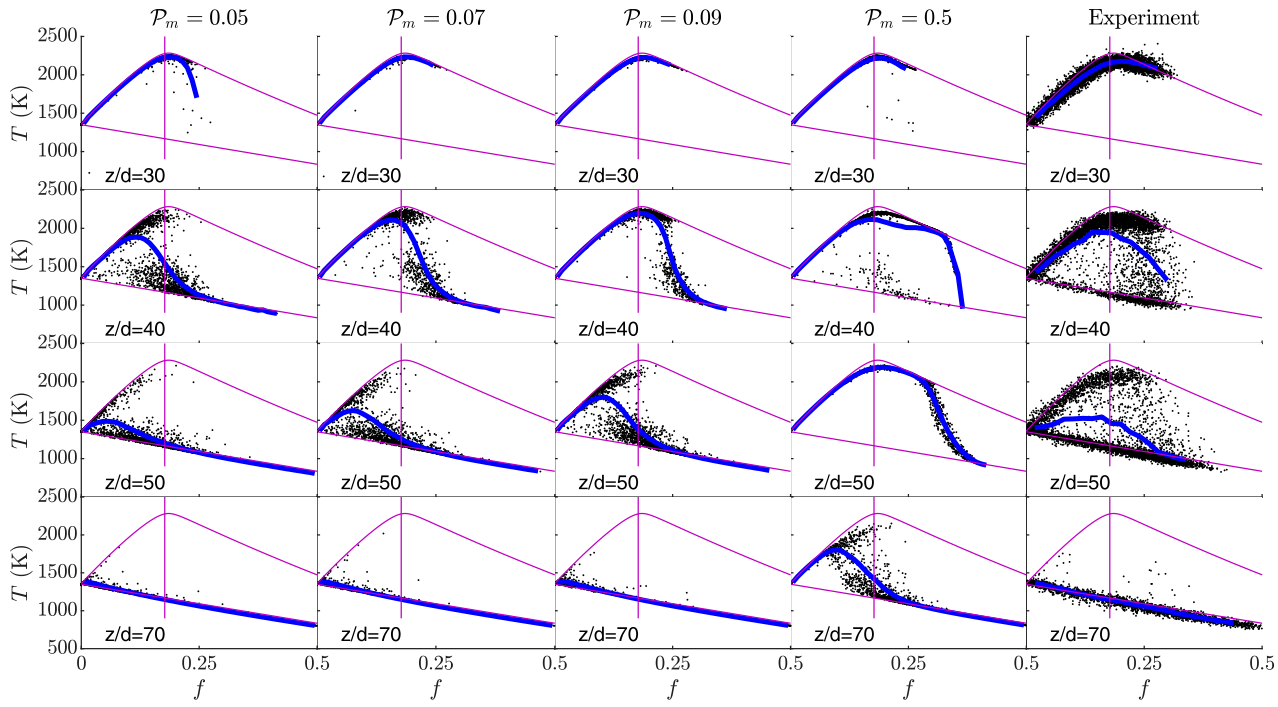

FIG. 25. Scatter plot of temperature vs mixture fraction for BLM-MMC. Each column has the same values of $\mathcal{P}_m$ as Fig. 24. There are 2500 randomly selected data points shown at various stations. Conditional temperature $\langle T|Z\rangle$: —. Equilibrium (upper) and frozen (lower) limits, and stoichiometric mixture fraction (vertical line): —.

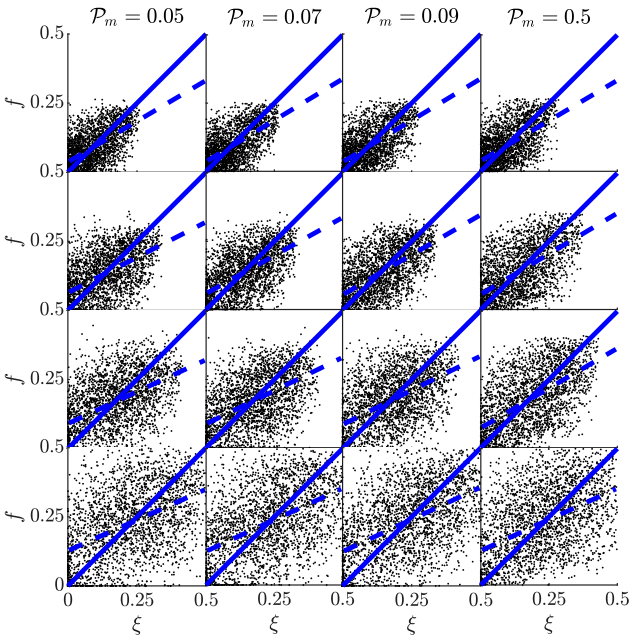

FIG. 26. Scatter plot of mixture fraction vs reference variable for BLM-MMC. The values of $\mathcal{P}_m$ and stations align with Fig. 25. There are 2500 randomly selected data points. Theoretical —; Linear least squares curve fit – –.

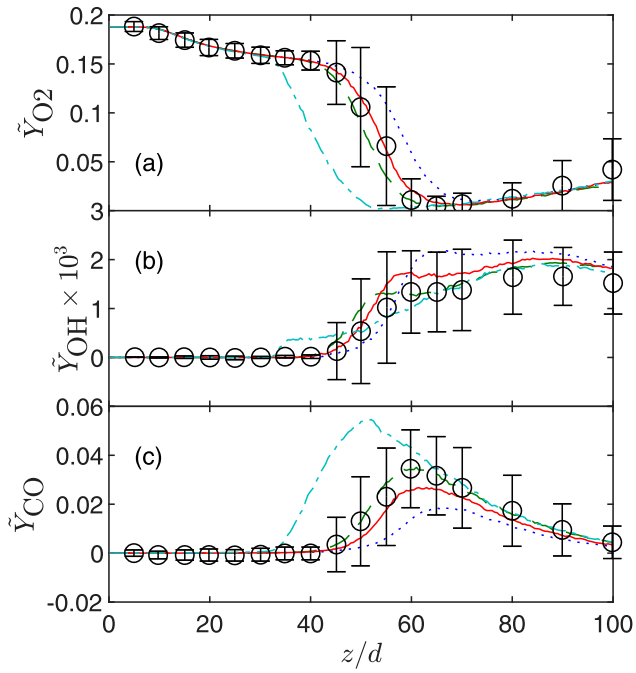

FIG. 27. Ensemble mean of centerline Favre-averaged mass fraction for the different fractions of particles mixing $\mathcal{P}_m$ in Fig. 24. (a) Molecular oxygen (O_2); (b) hydroxyl radical (OH); (c) carbon monoxide (CO). Lines: BLM-MMC; Experiment,[27] – °.

The mean amount of mixing used in the Modified Curl's model should be the intermediate value 0.5: decreasing the intensity generates too little local extinction by significantly advancing ignition, while increasing it causes the extinction/reignition process to occur too quickly due to retarded ignition. The results appear to be largely insensitive to the distribution used for the amount of mixing. The maximum mixing distance between particles, $\mathcal{L}$, influences the results in a similar fashion to C_Z, and the value $\mathcal{L} = \sqrt{B\Delta t}$ appears to be optimal. Although the diffusion length scale (the mean distance a particle moves in reference space within a time step) is physically $\sqrt{2B\Delta t}$, it appears that $\mathcal{L}$ needs to be smaller to reflect the mean distance over which particles interact within a time step. The fraction of particles to be mixed, $\mathcal{P}_m$, remains an unclosed parameter, and only the combustion behavior is sensitive to this parameter (by contrast, the mixture fraction statistics are relatively insensitive). Increasing $\mathcal{P}_m$ advances the flame by accelerating the ignition process. For the current case, the value of $\mathcal{P}_m = 0.07$ was determined to be optimal, but this was only determined *a posteriori* and is not expected to be a universal value. The ratio between the minor and major dissipation timescales varied with distance downstream and was much larger than the constant value of 1/8 that is commonly used.

Future work will investigate the methods for specifying $\mathcal{P}_m$ either *a priori* or *in situ*. Forcing the simulations to achieve a specified ratio between the minor and major dissipation timescales by controlling the mixing to achieve the required ratio of conditional and unconditional fluctuations is the best prospect for closing $\mathcal{P}_m$. Further work will also investigate the impact of age bias when selecting particle pairs, which is useful when modeling slow-chemistry effects such as soot and NO_x formation.

ACKNOWLEDGMENTS

Authors M. D. P. and D. B.-O. were each funded by an Australian Postgraduate Award. This research was undertaken using the University of Southern Queensland (USQ) Fawkes HPC, which is co-sponsored by QCIF (Queensland Cyber Infrastructure Foundation)—www.usq.edu.au/hpc.

DATA AVAILABILITY STATEMENT

The data that support the findings of this study are available from the corresponding author upon reasonable request.

REFERENCES

[1]D. J. Beerer and V. G. McDonell, "Autoignition of Hydrogen and Air Inside a Continuous Flow Reactor With Application to Lean Premixed Combustion", J. Eng. Gas Turbines Power **130**, 051507 (2008).
[2]D. Ahrens, M. Kolb, C. Hirsch, and T. Sattelmayer, "NOx Formation in a Reacting Premixed Jet in Hot Cross Flow", in *Proceedings of the ASME Turbo Expo 2014: Turbine Technical Conference and Exposition. Volume 4B: Combustion, Fuels and Emissions* (ASME, 2014).
[3]W. Qian, M. Zhu, and S. Li, "A Kinetics Study on the NOx Emissions of Axially Staged Combustion System for Gas Turbine Applications", in *Proceedings of Shanghai 2017 Global Power and Propulsion Forum* (GPPS, 2017).
[4]S. Li, W. Qian, H. Liu, G. Liu, and M. Zhu, "Autoignition and flame lift-off behavior of a fuel jet mixing with turbulent hot air coflow", in *Proceedings of the Combustion Institute* (Elsevier, 2020), p. 1540.
[5]W. Konrad, N. Brehm, F. Kameier, C. Freeman, and I. J. Day, "Combustion Instability Investigations on the BR710 Jet Engine", J. Eng. Gas Turbines Power **120**, 34 (1998).
[6]J. Eckstein, E. Freitag, C. Hirsch, T. Sattelmayer, and J. Eng, "Experimental Study on the Role of Entropy Waves in Low-Frequency Oscillations in a RQL Combustor", Gas Turbines Power **128**, 264 (2006).
[7]G. Vignat, E. L. Schiavo, D. Laera, A. Renaud, L. Gicquel, D. Durox, and S. Candel, "Dynamics of spray and swirling flame under acoustic oscillations: A joint experimental and LES investigation", in *Proceedings of the Combustion Institute* (Elsevier, 2020).
[8]F. Baillot, C. Patat, M. Cáceres, J.-B. Blaisot, and E. Domingues, "Saturation phenomenon of swirling spray flames at pressure antinodes of a transverse acoustic field", in *Proceedings of the Combustion Institute* (Elsevier, 2020).
[9]K. M. Lyons, "Toward an understanding of the stabilization mechanisms of lifted turbulent jet flames: {Experiments}", Prog. Energy Combust. Sci. **33**, 211 (2007).
[10]G. Coppola, B. Coriton, and A. Gomez, "Highly Turbulent Counterflow Flames: {A} Laboratory Scale Benchmark for Practical Systems", Combust. Flame **156**, 1834 (2009).
[11]Y. Shoshin and J. Jarosinski, "On Extinction Mechanism of Lean Limit Methane—Air Flame in a Standard Flammability Tube", Proc. Combust. Inst. **32**, 1043 (2009).
[12]U. Do Lee, C. S. Yoo, J. H. Chen, and J. H. Frank, "Effects of {H$–2$O} and {NO} on Extinction and Re-ignition of Vortex-Perturbed Hydrogen Counterflow Flames", Proc. Combust. Inst. **32**, 1059 (2009).
[13]S. Delhaye, L. M. T. Somers, J. A. van Oijen, and L. P. H. de Goey, "Incorporating Unsteady Flow-effects Beyond the Extinction Limit in Flamelet-generated Manifolds", Proc. Combust. Inst. **32**, 1051 (2009).
[14]A. Giusti and E. Mastorakos, "Turbulent Combustion Modelling and Experiments: Recent Trends and Developments", Flow, Turbul. Combust. **103**, 847 (2019).
[15]C. Dopazo and E. O'Brien, "An approach to the autoignition of a turbulent mixture", Acta Astronaut. **1**, 1239 (1974).
[16]C. Dopazo and E. O'Brien, "Functional formulation of nonisothermal turbulent reactive flows", Phys. Fluids **17**, 1968 (1974).
[17]N. Peters, "Multiscale Combustion and Turbulence", Proc. Combust. Inst. **32**(1), 1 (2009).
[18]S. B. Pope, "Small Scales, Many Species and the Manifold Challenges of Turbulent Combustion", Proc. Combust. Inst. **34**(1), 1 (2013).
[19]S. B. Pope, "The Probability Approach to the Modelling of Turbulent Reacting Flows", Combust. Flame **27**, 299 (1976).
[20]R. Lindstedt, S. Louloudi, J. Driscoll, and V. Sick, "Finite Rate Chemistry Effects in Turbulent Reacting Flows", Flow, Turbul. Combust. **72**, 407 (2004).
[21]Z. Ren and S. B. Pope, "An investigation of the performance of turbulent mixing models", Combust. Flame **136**, 208 (2004).
[22]A. Y. Klimenko and S. B. Pope, "The modeling of turbulent reactive flows based on multiple mapping conditioning", Phys. Fluids **15**, 1907 (2003).
[23]M. J. Cleary and A. Y. Klimenko, "Multiple Mapping Conditioning: A New Modelling Framework for Turbulent Combustion", in *Turbulent Combustion Modeling*, edited by T. Echekki and E. Mastorakos (Springer, 2011), pp. 143–173.
[24]S. K. Ghai, S. De, K. Vogiatzaki, and, and M. J. Cleary, "Theory and Application of Multiple Mapping Conditioning for Turbulent Reactive Flows", in *Modeling and Simulation of Turbulent Combustion*, Energy, Environment, and Sustainability, edited by S. De, A. K. Agarwal, S. Chaudhuri, and S. Sen (Springer, Singapore, 2018), pp. 447–474.
[25]A. P. Wandel, "A Physical Understanding of how Multiple Mapping Conditioning Works", in *Proceedings of the 2019 Australian Combustion Symposium*, Invited Talk edited by P. Medwell, Z. Alwahabi, M. Evans, S. Chan, A. Chinnici, Z. Tian, and B. Dally (The University of Adelaide, 2019), pp. 20–27.
[26]R. S. Barlow and J. Frank, "Effects of Turbulence on Species Mass Fractions in Methane/Air Jet Flames", Proc. Combust. Inst. **27**, 1087 (1998).
[27]R. Cabra, J.-Y. Chen, R. W. Dibble, A. N. Karpetis, and R. S. Barlow, "Lifted methane–air jet flames in a vitiated coflow", Combust. Flame **143**, 491 (2005).
[28]Y. Ge, M. J. Cleary, and A. Y. Klimenko, "Sparse-Lagrangian FDF simulations of Sandia Flame E with density coupling", Proc. Combust. Inst. **33**, 1401 (2011).
[29]A. P. Wandel and R. P. Lindstedt, "Hybrid multiple mapping conditioning modeling of local extinction", Proc. Combust. Inst. **34**, 1365 (2013).

[30]K. Vogiatzaki, S. Navarro-Martinez, S. De, and A. Kronenburg, "Mixing Modelling Framework Based on Multiple Mapping Conditioning for the Prediction of Turbulent Flame Extinction", Flow, Turbul. Combust. **95**, 501 (2015).
[31]C. Straub, S. De, A. Kronenburg, and K. Vogiatzaki, "The effect of timescale variation in multiple mapping conditioning mixing of PDF calculations for Sandia Flame series D–F", Combust. Theory Modell. **20**, 894 (2016).
[32]A. Varna, M. J. Cleary, and E. R. Hawkes, "A multiple mapping conditioning mixing model with a mixture-fraction like reference variable. Part 2: RANS implementation and validation against a turbulent jet flame", Combust. Flame **181**, 354 (2017).
[33]A. P. Wandel and R. P. Lindstedt, "A mixture-fraction-based hybrid binomial Langevin-multiple mapping conditioning model", Proc. Combust. Inst. **37**, 2151 (2019).
[34]S. K. Ghai and S. De, "Numerical investigation of auto-igniting turbulent lifted CH4/air jet diffusion flames in a vitiated co-flow using a RANS based stochastic multiple mapping conditioning approach", Combust. Flame **203**, 362 (2019).
[35]S. B. Pope, "Accessed Compositions in Turbulent Reactive Flows", Flow, Turbul. Combust. **72**, 219 (2004).
[36]A. Y. Klimenko and R. W. Bilger, "Conditional moment closure for turbulent combustion", Prog. Energy Combust. Sci. **25**, 595 (1999).
[37]A. Y. Klimenko, "Modern modeling of turbulent premixed combustion and reduction of pollution emissions", Clean Air **7**, 14.4 (2003).
[38]A. P. Wandel and A. Y. Klimenko, "Testing multiple mapping conditioning mixing for Monte Carlo probability density function simulations", Phys. Fluids **17**, 128105 (2005).
[39]A. P. Wandel, "Conditional dissipation of scalars in homogeneous turbulence: Closure for MMC modelling", Combust. Theory Modell. **17**, 707 (2013).
[40]A. Y. Klimenko, "Matching the conditional variance as a criterion for selecting parameters in the simplest multiple mapping conditioning models", Phys. Fluids **16**, 4754 (2004).
[41]M. J. Cleary, A. Y. Klimenko, J. Janicka, and M. Pfitzner, "A sparse-Lagrangian multiple mapping conditioning model for turbulent diffusion flames", Proc. Combust. Inst. **32**, 1499 (2009).
[42]L. Valiño and C. Dopazo, "A binomial Langevin model for turbulent mixing", Phys. Fluids A **3**, 3034 (1991).
[43]A. P. Wandel and R. P. Lindstedt, "Hybrid binomial Langevin-multiple mapping conditioning modeling of a reacting mixing layer", Phys. Fluids **21**, 015103 (2009).
[44]C. Dopazo, "Relaxation of initial probability density functions in the turbulent convection of scalar fields", Phys. Fluids **22**, 20 (1979).
[45]J. Janicka, W. Kolbe, and W. Kollmann, "Closure of the Transport Equation for the Probability Density Funcfion of Turbulent Scalar Fields", J. Non-Equilib. Thermodyn. **4**, 47 (1979).
[46]D. B. Spalding, "Concentration fluctuations in a round turbulent free jet", Chem. Eng. Sci. **26**, 95 (1971).
[47]S. Mitarai, J. J. Riley, and G. Kosály, "A Lagrangian study of scalar diffusion in isotropic turbulence with chemical reaction", Phys. Fluids **15**, 3856 (2003).
[48]S. Mitarai, J. J. Riley, and G. Kosály, "Testing of mixing models for Monte Carlo probability density function simulations", Phys. Fluids **17**, 047101 (2005).
[49]T. Hůlek and R. P. Lindstedt, "Joint Scalar-velocity pdf Modelling of Finite Rate Chemistry in a Scalar Mixing Layer", Combust. Sci. Technol. **136**, 303 (1998).
[50]R. Curl, "Dispersed phase mixing: I. Theory and effects in simple reactors", AIChE J. **9**, 175 (1963).
[51]A. Varna, M. J. Cleary, and E. R. Hawkes, "A multiple mapping conditioning mixing model with a mixture-fraction like reference variable. Part 1: Model derivation and ideal flow test cases", Combust. Flame **181**, 342 (2017).
[52]S. K. Ghai, S. De, and A. Kronenburg, "Numerical simulations of turbulent lifted jet diffusion flames in a vitiated coflow using the stochastic multiple mapping conditioning approach", Proc. Combust. Inst. **37**, 2199 (2019).
[53]A. P. Wandel, "Development of multiple mapping conditioning (MMC) for application to turbulent combustion," Ph.D. thesis, Division of Mechanical Engineering, The University of Queensland, 2005.
[54]K. Gkagkas and R. P. Lindstedt, "Transported PDF modelling with detailed chemistry of pre- and auto-ignition in CH4/air mixtures", Proc. Combust. Inst. **31**, 1559 (2007).
[55]R. R. Cao, S. B. Pope, and A. R. Masri, "Turbulent lifted flames in a vitiated coflow investigated using joint PDF calculations", Combust. Flame **142**, 438 (2005).